THE ASTROPHYSICAL JOURNAL, 441:644–664, 1995 March 10

THE STABILITY AND COLLIMATION OF THREE-DIMENSIONAL JETS

PHILIP E. HARDEE
Department of Physics and Astronomy, University of Alabama, Tuscaloosa, AL 35487
DAVID A. CLARKE
Department of Astronomy and Physics, Saint Mary's University, Halifax, NS, Canada B3H 3C3
AND
D. ANDREW HOWELL
University of Florida, Department of Astronomy, Gainesville, FL 32611
Received 1994 April 22; accepted 1994 September 21

ABSTRACT

A three-dimensional hydrodynamical simulation of a Mach 5 cylindrical jet established in equilibrium with a surrounding uniform atmosphere of 10 times the jet density has been performed and is compared with a previous Mach 3 simulation. The grid resolution used is significantly higher than was used in the previous simulation of a Mach 3 equilibrium jet. The higher resolution has not significantly changed the development of large-scale structures such as the helical twisting of the jet, the elliptical distortion and bifurcation of the jet, or the triangular distortion and trifurcation of the jet seen in the lower resolution simulation. These structures arise from the Kelvin-Helmholtz unstable surface modes predicted by the linear theory, and the elliptical mode appears coupled to the precessionally driven helical mode. Newly discovered is a short-wavelength, relatively large-amplitude transverse velocity oscillation on the jet axis. The effect of the unstable body modes on jet structure is analyzed for the first time, and a helical internal body mode is revealed to be responsible for the observed short-wavelength velocity oscillation on the jet axis. This body mode helically twists the inner 20%–25% of the jet, and the transverse velocity oscillation occurs at the fastest spatially growing wavelength predicted by the theory. While the higher resolution of the new simulation has allowed the development of structures on smaller scales and reveals more detail, large-scale surface distortion and accompanying surface filamentation still appear to dominate jet dynamics, and decollimation occurs as the helically distorted jet bifurcates or trifurcates. This newer simulation suggests that mass entrainment, and significant shock heating and dissipation, occur as the jet breaks up into multiple streams, and qualitative comparison between the two simulations suggests that more shock heating and decollimation occur in the Mach 5 simulation.

Subject headings: hydrodynamics — ISM: jets and outflows — shock waves

1. INTRODUCTION

A large number of effectively two-dimensional numerical simulations have been performed over the past few years (see Norman 1993 for a review). The two-dimensional simulations have established the qualitative behavior of highly collimated outflows in situations of astrophysical interest, e.g., the jets associated with extragalactic radio sources. The numerical simulations (Norman, Winkler, & Smarr 1984) have shown that jets must be much less dense than the surrounding medium if they are to produce the large lobes seen in radio sources of Fanaroff-Riley II (FR II) type. In the jet simulations in constant atmospheres the jet resides within a lobe formed by back-flowing material that is less dense than the jet. The stability properties of the highly collimated jet influence the morphology. For the case of a jet inside a lobe, large-scale sideways motion of the jet can destroy the collimation before the jet reaches the outer extent of the lobe (Hardee & Norman 1990). If this occurs, leading-edge hot spots can no longer be formed. The numerical simulations have also shown that atmospheric gradients can influence jets of low power and Mach number with density somewhat less than the density in the external medium, to form a more taillike structure reminiscent of FR I type radio sources. In these simulations atmospheric gradients prevent strong backflows, and the jet can interact directly with a denser external medium. While sideways motion also destroys jet collimation, in this case the combination of declining pressure and density in the atmosphere and jet density comparable to the density in the atmosphere can allow long tails to form (Hardee et al. 1992b). In general, the behavior of the two-dimensional numerical simulations performed in slab geometry which allowed nonaxisymmetric motion demonstrated unstable behavior that was fully consistent with a linearized analysis of the time-dependent magnetofluid equations (Hardee & Norman 1988; Norman & Hardee 1988; Hardee et al. 1992a).

More recently it has become possible to perform three-dimensional numerical simulations with resolution sufficient to begin study of the highly collimated jets observed in extragalactic radio sources. A simulation of a jet propagating through a transonic cross flow (Balsara & Norman 1992) has shown how a collimated jet might bend and disrupt as the result of galaxy motion in a cluster. The effect of precession and resulting helical twisting of a propagating jet has been used to reveal how multiple hot spots can be formed at the leading edge of the lobes in FR II type radio sources (Cox, Gull, & Scheuer 1991). In another simulation the interaction of a propagating jet with a cloud has been explored (Clarke 1993). As a by-product of the jet-cloud interaction, a lobe was formed which showed filamentary structures like those seen in the lobes of FR II type radio sources. In order to begin an investigation of the smaller scale structures that might be formed far behind the leading edge of a jet, where an approximate equi-

librium has been achieved, Hardee & Clarke (1992) performed an equilibrium jet simulation. In an equilibrium simulation the jet is established across the computational grid at the beginning of the simulation. Such a simulation removes effects such as the interaction of a jet with back-flowing lobe material or lobe turbulence, and is well suited to studying jet structure far behind any leading edge. Additionally, this type of simulation is uniquely suited to a study of the structures predicted by a linearized analysis of the time-dependent magnetofluid equations because the initial conditions in the external medium are not modified by a bow shock. In general, such an analysis suggests that a highly collimated outflow is much more unstable in three dimensions than in two dimensions. This is a result of additional unstable modes that do not exist in two dimensions (see Birkinshaw 1991 for a review). The additional unstable modes also provide additional structures related to flow properties that should appear on extragalactic jets.

In a previous equilibrium jet simulation Hardee & Clarke (1992) found large-scale structures such as helical twisting of the flow, elliptical distortion and bifurcation of the flow, and triangular distortion and trifurcation of the flow that appeared to be related to the unstable surface Kelvin-Helmholtz normal modes predicted by the linear theory. However, with 20 grid zones across the jet diameter, internal jet structure and mixing processes at the jet surface were insufficiently resolved. Additionally, the low Mach number meant that all of the regular structures observed were fully developed on an axial scale of 20 jet radii, which occupied only the first third of the computational grid. In order to address the effect of grid resolution on the larger scale jet structures found previously, and in an attempt to look for internal jet structure such as might be produced by the body modes predicted by the linear theory, a second numerical simulation with significantly higher grid resolution in the radial direction has been performed. The axial distance has been reduced, and as a result somewhat higher grid resolution in the axial direction is achieved. The Mach number has been increased in order to allow evaluation of the dependence of jet instability on the Mach number.

2. NUMERICAL SIMULATION

2.1. *Initial Setup*

The simulation was performed using the three-dimensional MHD code ZEUS-3D based on the ZEUS code described in Norman & Winkler (1986), Clarke, Norman, & Burns (1989), and Stone & Norman (1992a, b). In the ZEUS code the second-order–accurate monotonic van Leer (1977) interpolation algorithm is used for the advective terms in the conservation equations. Shocks are handled by the usual von Neumann–Richtmyer artifical viscosity, which will typically smear a shock over several grid zones. The simulation is initialized by establishing a cylindrical jet across a three-dimensional Cartesian grid of dimension $100 \times 100 \times 300$. In this simulation 30 uniform zones span the jet diameter along the transverse Cartesian axes, and 300 uniform zones span a distance of 45 times the jet radius in the axial direction. Outside the jet the zones are ratioed so that the 100 transverse zones span a total distance of 18 times the jet radius along the transverse Cartesian axes. In the previous simulation 20 uniform zones spanned the jet diameter, 100 transverse zones spanned a total distance of 26 times the jet radius along the transverse Cartesian axes, and 300 uniform zones spanned a distance of 60 times the jet radius in the axial direction.

As in the previous simulation, the jet is pressure-matched to the external medium, which has a density 10 times that of the jet. In this simulation the relevant Mach numbers are $M_j \equiv u/a_j = 5.0$ and $M_x \equiv u/a_x = 15.8$, where a_j and a_x are sound speeds in the jet and in the external medium, respectively, and u is the jet velocity. In the previous simulation the Mach numbers were $M_j \equiv u/a_j = 3.0$ and $M_x \equiv u/a_x = 9.5$. In both simulations the cylindrical jet is initialized with a solid-body angular rotation equal to $0.001u$ at the jet surface to help smooth the effects of the Cartesian grid, and densities and velocities are averaged in zones not filled exclusively by jet or external material. In both simulations the cylindrical jet is driven by a periodic precession of the jet velocity at an angle of 0.01 radians relative to the axial direction at the inlet. In the previous and present simulations the periodic precession has an angular frequency $\omega R/a_x = 1.0$ and $\omega R/a_x = 1.6$, respectively, where R is the jet radius. The direction of precession opposes the angular solid-body rotation. Outflow boundary conditions are used except where the jet enters the grid. The jet goes through three phases of evolution in the $\tau \equiv t(a_x/R) = 12$ dynamical times of the simulation, and these three phases are illustrated by examining the simulation in detail at dynamical times $\tau = 3$, 6, and 12. A similar evolution is observed in the Mach 3 simulation.

2.2. *Dynamical Time* $\tau = 3$

One-dimensional slices along the jet axis of the axial velocity (1-velocity) and Mach number, and the transverse orthogonal 2-velocity and 3-velocity components, are shown in Figure 1. The 1-velocity shows a periodic fluctuation with wavelength $\sim 5R$ and an exponential decrease in the minimum axial velocity as $u = u_0 - Ae^{z/l}$, where $A = 0.0048$ and $l = 4.0$, to a minimum at an axial distance $z = 30R$, at which point the internal Mach number has dropped to 1. The transverse velocity components show a sinusoidal oscillation with wavelength $\sim 10R$ and amplitude $\sim a_x$ between 20 and 35 jet radii from the origin, coincident with the periodic fluctuation of the 1-velocity but with twice the wavelength. These transverse motions along orthogonal axes are in phase and of approximately the same amplitude, indicating an overall transverse sinusoidal oscillation of the jet along an axis at a 45° angle to the Cartesian axes. Smaller scale sinusoidal velocity substructure with wavelength $\sim 5R$ and amplitude $\sim a_x/4$ is superposed on the larger amplitude and wavelength sinusoidal velocity oscillation in the transverse directions. That the longer wavelength transverse oscillation is sinusoidal and not helical is illustrated by the axial vector velocity slices in orthogonal planes along the 2- and 3-axes shown in Figure 2, and by the axial temperature slices in orthogonal planes along the 2- and 3-axes shown in Figure 3. These slices indicate an in-phase transverse motion along the 2- and 3-axes. The axial temperature slices also show that a symmetric pinching perturbation is responsible for the fluctuation in the 1-velocity with wavelength $\sim 5R$ and the decrease in the axial velocity to the minimum at an axial distance of $30R$.

Figure 4 shows six transverse temperature slices at axial distances from $7.5R$ to $45R$ in $7.5R$ intervals. The transverse slices show relatively high-order fluting of the cylindrical jet inside $15R$, a distinct four-lobed flute at $30R$, and only small disturbance at larger axial distance at this early time. An isotemperature surface (Fig. 5) shows little evidence for twisting of the high-order fluting at axial distance less than $20R$ but suggests some twist in the four-lobe fluting at an axial distance of

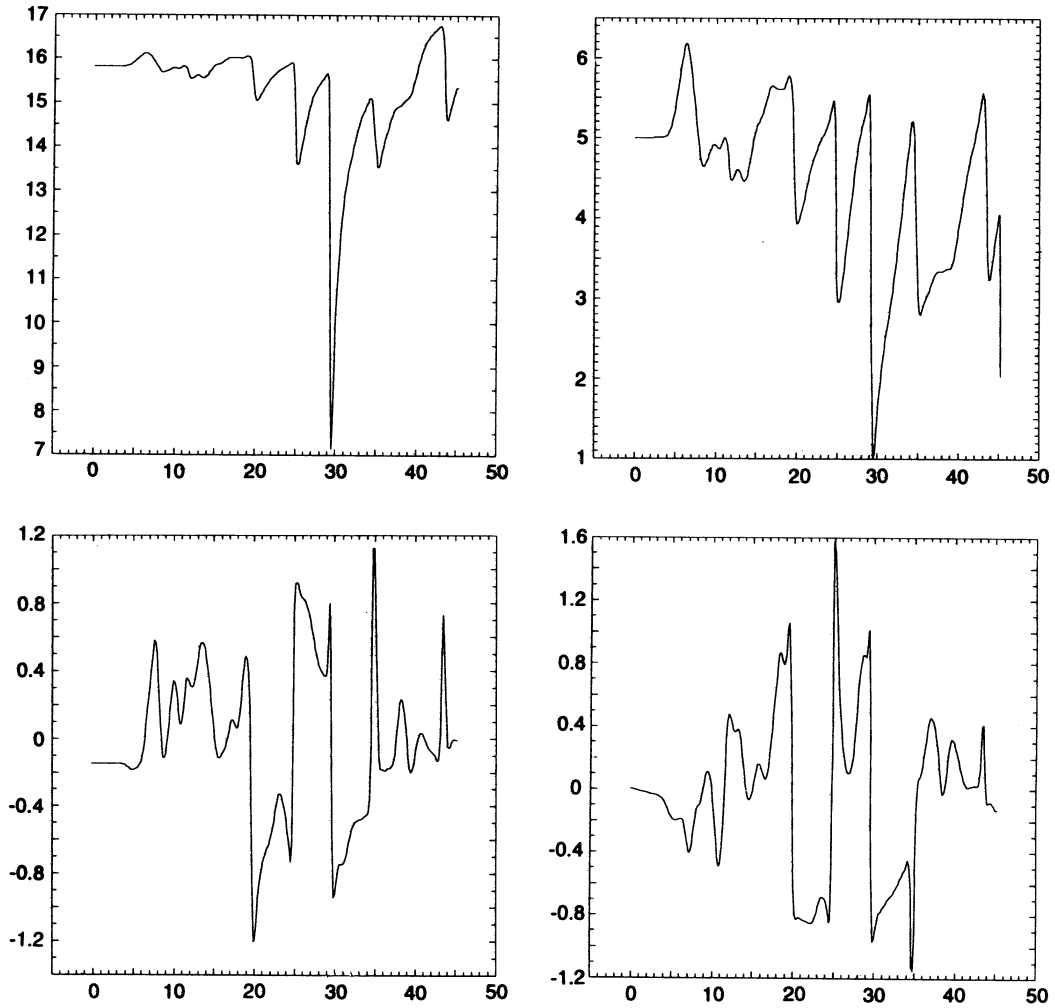

FIG. 1.—Axial 1-velocity (*top left*) and Mach number (*top right*), and transverse orthogonal 2-velocity (*bottom left*) and 3-velocity (*bottom right*) components along the jet axis at dynamical time $\tau = 3$. Velocities are scaled relative to the sound speed in the medium external to the jet, and the axial distance is scaled relative to the jet radius.

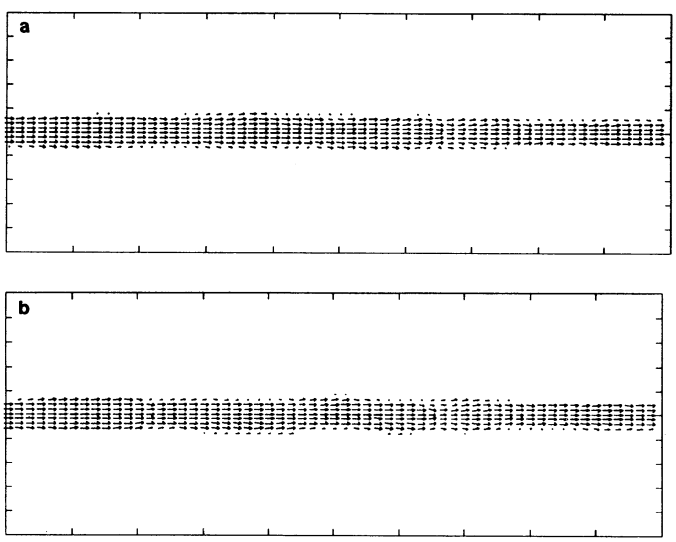

FIG. 2.—Vector velocities on orthogonal planes through the jet axis at time $\tau = 3$, (*a*) in the (1-axis, 2-axis)-plane and (*b*) in the (1-axis, 3-axis)-plane.

30*R*. At 30*R* and at larger axial distance, a pinch can be seen in the isotemperature surface that corresponds to the pinching evident in the axial vector velocity slices (Fig. 2) and in the axial temperature slices (Fig. 3). Two orthogonal line-of-sight integrations of the velocity divergence which indicate the position of shocks are shown in Figure 6. The lines of sight, *not along the* 2- *and* 3-*axes*, have been chosen to illustrate that symmetric pinch mode–associated conical shocks evident in Figure 6*a* coexist with an asymmetric sinusoidal oscillation evident in Figure 6*b*. The images show that the conical shock is asymmetric and stronger in one quadrant. Also evident at axial distances less than 15*R* are weaker, closely spaced multiple shocks. At this stage of the simulation, aside from the surface fluting, the jet shows behavior similar to previously performed slab jet simulations, in that the dominant features appear associated with pinching and sinusoidal oscillation. This initial slablike behavior does not last beyond dynamical time 3. Note that this dynamical time is about one flow through time, i.e., jet material entering the grid at $\tau = 0$ is just leaving the grid at $\tau \approx 3$, and the jet has precessed through about three-quarters of a revolution.

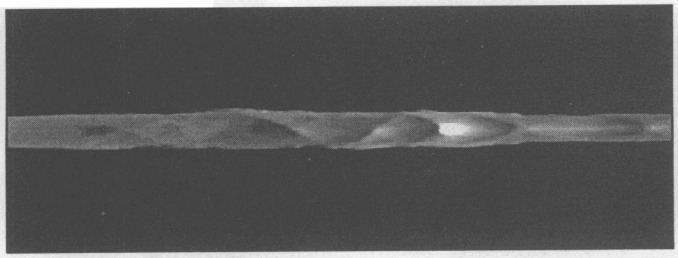

FIG. 3a

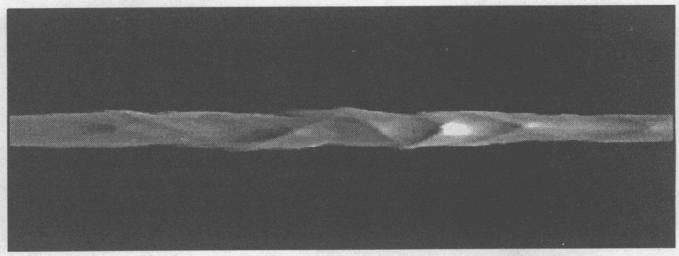

FIG. 3b

FIG. 3.—Gray-scale rendering of the temperature on orthogonal planes through the jet axis at time $\tau = 3$, (*a*) in the (1-axis, 2-axis)-plane and (*b*) in the (1-axis, 3-axis)-plane, corresponding to the vector velocities shown in Fig. 2. Lighter gray indicates higher temperature.

2.3. *Dynamical Time* $\tau = 6$

One-dimensional slices along the jet axis of the axial velocity (1-velocity) and Mach number, and the transverse 2-velocity and 3-velocity components, are shown in Figure 7. The axial velocity remains relatively constant out to an axial distance of $25R$ and then shows a velocity fluctuation with wavelength $\sim 10R$ superposed on an average linear decline. There is more variation in the Mach number, but the average Mach number remains constant out to an axial distance of $25R$, at which point the Mach number shows fluctuation similar to that seen in the axial velocity superposed on a linear decline. At $45R$ the axial velocity is about one-third of the velocity at the inlet and the Mach number is ~ 1.5. The 2-velocity shows an oscillation with wavelength $\sim 20R$ and amplitude growing from $\sim a_x/2$ at an axial distance of $\sim 15R$ to $\sim 2.5a_x$ at an axial distance of $\sim 35R$. The 3-velocity also shows an oscillation with similar wavelength and amplitude, but out of phase with the 2-velocity by $\sim 5R$. This phase difference is in accord with a helical twist of wavelength $\sim 20R$. Smaller scale sinusoidal velocity substructure with wavelength $\sim 5R$ and amplitude $\sim a_x$ is superposed on the larger amplitude and wavelength sinusoidal velocity oscillation in the transverse directions. This short-wavelength transverse oscillation is out of phase along the 2- and 3-axes by $\sim R$, and this is consistent with a helical twist of wavelength $\sim 5R$. The complexity of the flow is partially revealed by the axial vector velocity slices along the 2- and 3-axes shown in Figure 8, and by axial temperature slices along the 2- and 3-axes shown in Figure 9. Both axial vector velocity slices and temperature slices show oscillation indicative of helical twisting. Equally prominent is a narrowing of the flow along one transverse axis, accompanied by a broadening of the flow along the orthogonal transverse axis. This observed structure is indicative of elliptical distortion. The spatial scale along one axis from broadening to narrowing back to broadening is $\sim 14R$.

Spatial development of perturbations to the jet boundary is revealed further by the transverse temperature slices shown in Figure 10. At an axial distance of $7.5R$ the jet shows relatively high-order small-scale surface fluting similar to that at the earlier dynamical time. At larger axial distance the transverse

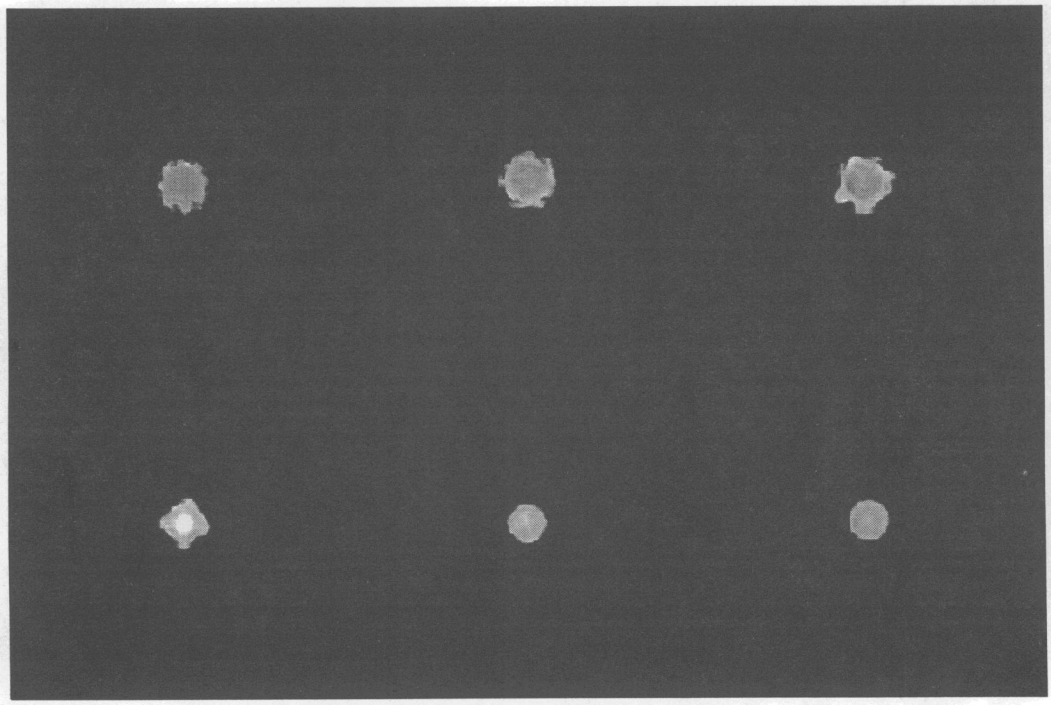

FIG. 4.—Gray-scale rendering of the temperature on two-dimensional planes orthogonal to the jet axis at distances from 7.5 to 45 jet radii in increments of 7.5 jet radii, from top left to bottom right, at time $\tau = 3$. Lighter gray indicates higher temperature.

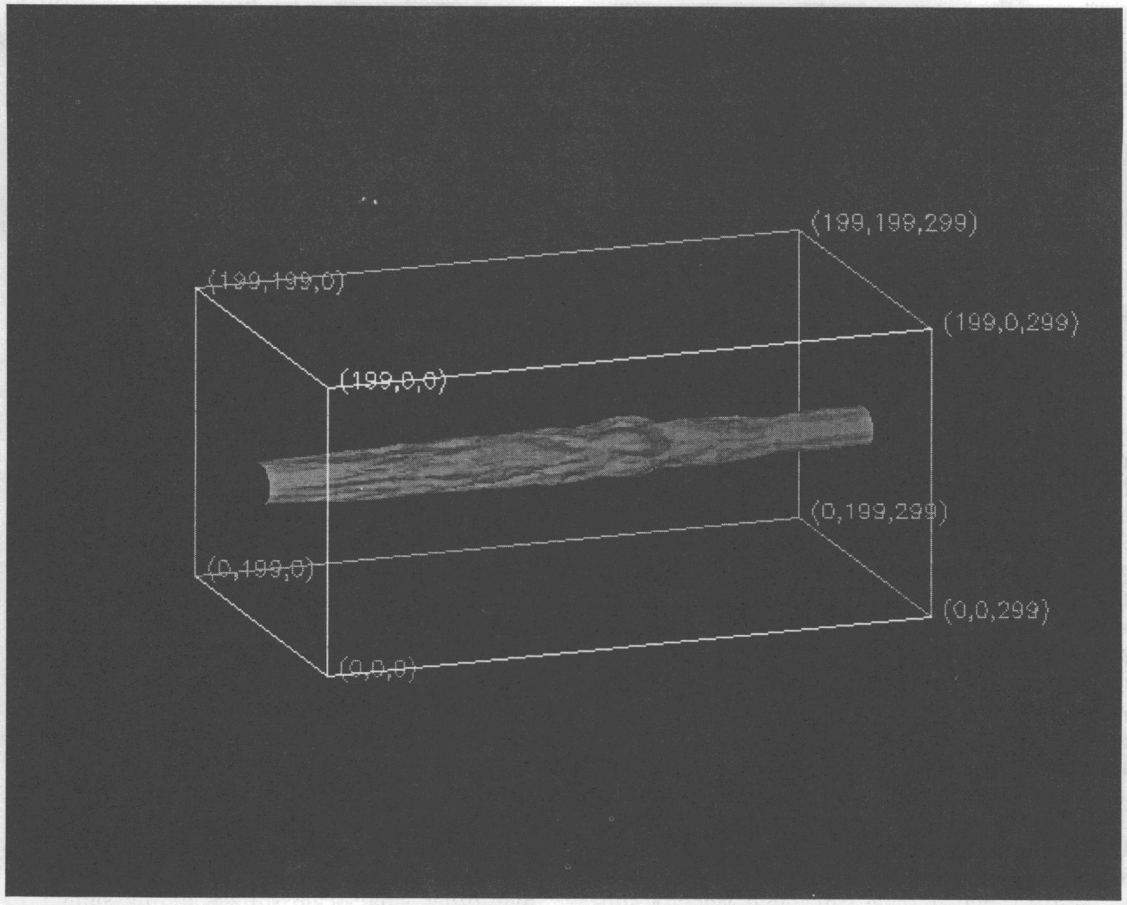

FIG. 5.—Isotemperature surface separating the hot jet material from the cooler external material at time $\tau = 3$.

structure is dominated by much larger scale distortion. At axial distance $30R$ jet flattening is evident, and at $37.5R$ the jet breaks up into filaments. The smaller disturbance at $45R$ indicates that a steady state has not yet been reached at this dynamical time. Note that a dynamical time of $\tau = 6$ would correspond to about two flow-through times if the axial velocity remained constant across the grid, and the precession at the origin has completed about 1.5 revolutions. Two isotemperature surfaces are shown in Figure 11. The inner, higher temperature isosurface shows the large-scale helicity suggested by the transverse velocity structure and by the axial temperature slices. The outer, lower temperature isosurface reveals that the initial highly collimated flow has broadened significantly at axial distances larger than $15R$. Two orthogonal line-

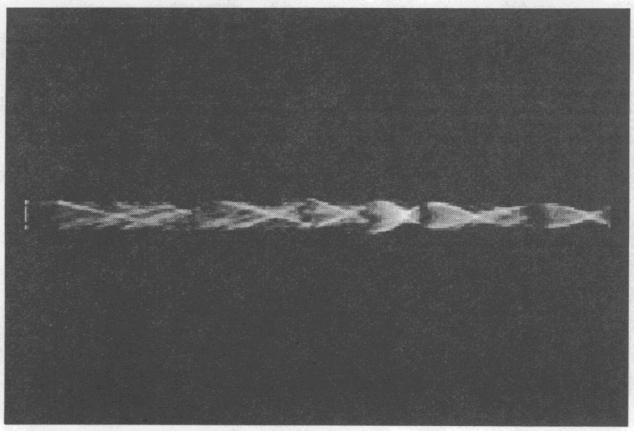

FIG. 6*a*

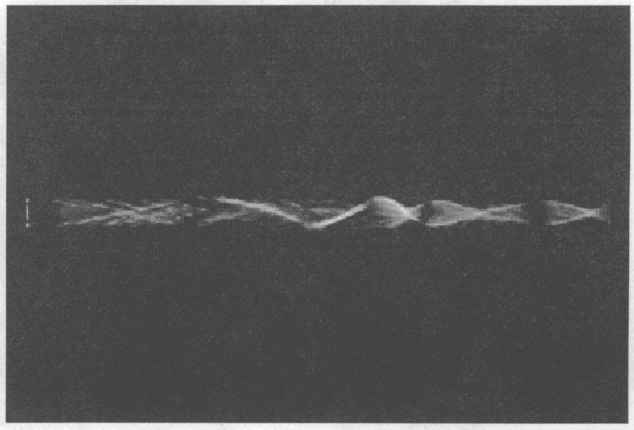

FIG. 6*b*

FIG. 6.—Ray integrations along orthogonal axes (*not the* 2- *and* 3-*axes*) of the velocity divergence (indicates the location of shocks) through the data cube at time $\tau = 3$.

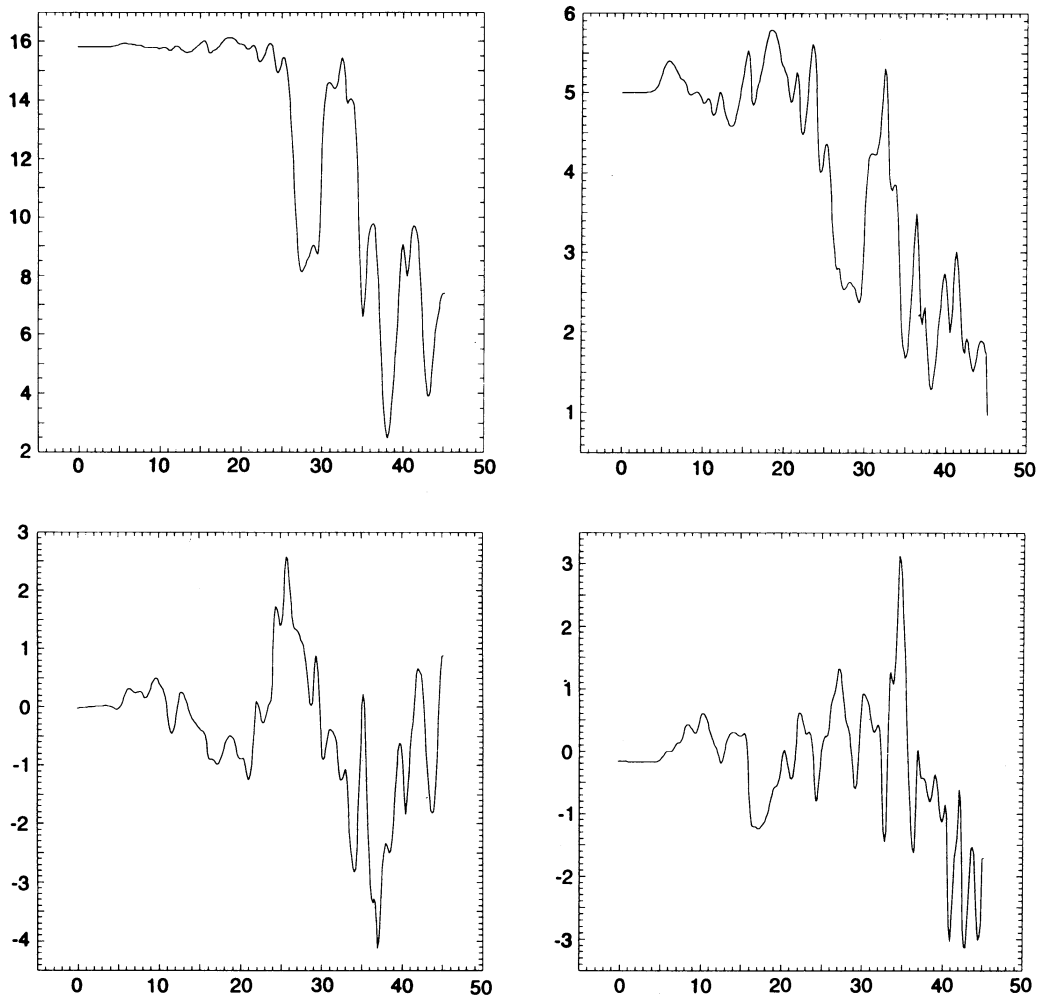

FIG. 7.—Axial 1-velocity (*top left*) and Mach number (*top right*), and transverse orthogonal 2-velocity (*bottom left*) and 3-velocity (*bottom right*) components along the jet axis at dynamical time $\tau = 6$. Velocities are scaled relative to the sound speed in the medium external to the jet, and the axial distance is scaled relative to the jet radius.

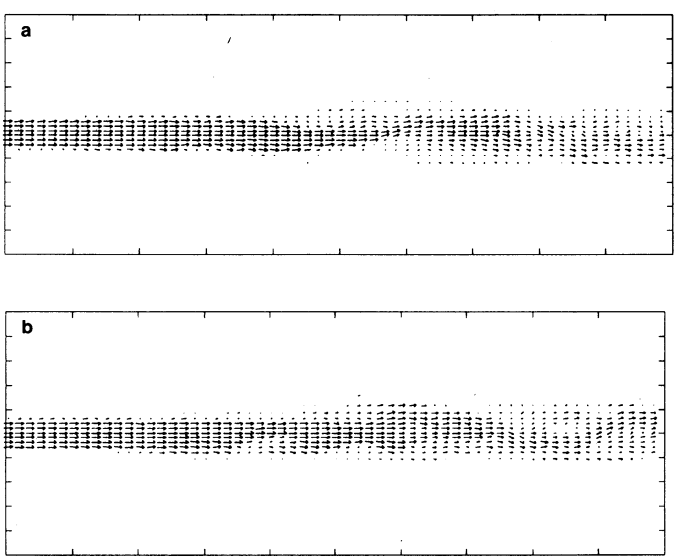

FIG. 8.—Vector velocities on orthogonal planes through the jet axis at time $\tau = 6$, (*a*) in the (1-axis, 2-axis)-plane and (*b*) in the (1-axis, 3-axis)-plane.

of-sight integrations, *not along the* 2- and 3-*axes*, of the velocity divergence shown in Figure 12 show compressions that tend to wrap around the jet surface at axial distances beyond about 15*R*. At lesser axial distance, structures such as the three bright filaments in Figure 12*a* are definitely sheetlike, and hence are not apparent in the orthogonal image (Fig. 12*b*).

2.4. *Dynamical Time* $\tau = 12$

One-dimensional slices along the jet axis of the axial velocity), the Mach number, and the 2-velocity and 3-velocity components along with the specific energy (temperature) and the jet density, are shown in Figure 13. The axial velocity remains relatively constant out to a distance of 25*R*, then shows a sharp initial velocity drop and subsequent velocity fluctuation with wavelength $\sim 10R$ that is superposed on a slow linear decline that is similar to that seen at time $\tau = 6$. At 45*R* the axial velocity is about one-half of the velocity at the inlet. There is more variation in the Mach number than in the velocity, but the average Mach number remains constant out to an axial distance of 25*R*, at which point the Mach number shows a sharp drop and subsequent fluctuation similar to that seen in the axial velocity, and slow linear decline to a value at

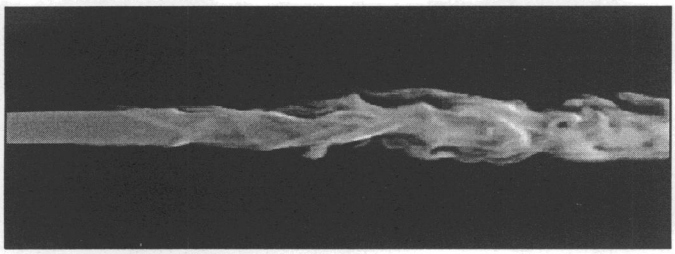

FIG. 9a

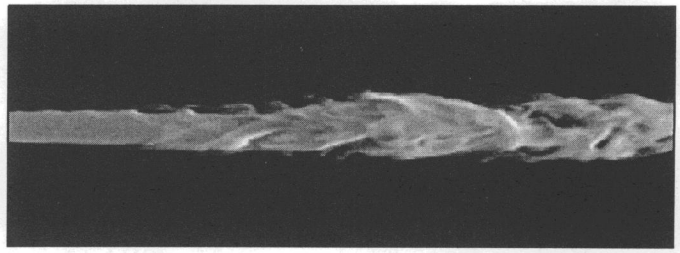

FIG. 9b

FIG. 9.—Gray-scale rendering of the temperature on orthogonal planes through the jet axis at time $\tau = 6$, (*a*) in the (1-axis, 2-axis)-plane and (*b*) in the (1-axis, 3-axis)-plane, corresponding to the vector velocities shown in Fig. 8. Lighter gray indicates higher temperature.

$45R$ slightly more than a factor of 2 less than the Mach number at the inlet. That the Mach number has decreased by a slightly larger factor than the axial velocity by $45R$ is a consequence of a slight increase in the temperature. The density along the axis has also declined by about a factor of 2 by $45R$. The 2-velocity shows sinusoidal substructure with wavelength $\sim 5R$ and growth in the magnitude of the 2-velocity from $\sim a_x$ to $\sim 2.5a_x$ between axial distances $15R$ and $30R$. Large-scale structure is suggested by typically positive velocities between $10R$ and $20R$ and negative velocities between $20R$ and $35R$. A large negative velocity spike at $\sim 26R$ is associated with the sharp reduction in axial velocity at $\sim 25R$. The 3-velocity shows similar sinusoidal substructure with wavelength $\sim 5R$ and growth in the magnitude of the 3-velocity from $\sim a_x$ to $\sim 4.5a_x$ between axial distances $15R$ and $35R$. The large positive velocity spike at $\sim 26R$ in the 3-velocity like the velocity spike in the 2-velocity is associated with the sharp velocity reduction in axial velocity at $\sim 25R$. Large-scale structure is suggested by typically negative velocities between $15R$ and $35R$ and positive velocities between $35R$ and $45R$ with magnitude $\geq a_x$. At this time velocity oscillation in the transverse direction at small wavelength ($\sim 5R$) exceeds the oscillation in the transverse direction at large wavelength ($\sim 20R$) by about a factor of 3.

Axial vector velocity slices along the 2- and 3-axes are shown in Figure 14, and axial temperature slices along the 2- and 3-axes are shown in Figure 15. The axial temperature slices show oscillation interior to axial distances of $25R$ indicative of helical twisting with a wavelength of $\sim 23R$. The raggedness of the borders in the temperature slices suggests mixing with external material at axial distances greater than $25R$. As at time $\tau = 6$, a prominent elliptical distortion of the flow can be seen. In this case the distortion accompanies the rapid jet slowing at $25R$ and has a spatial scale on the order of $10R$ (Fig. 14). This structure is also evident in the axial temperature slices. Spatial development of the jet surface is revealed in Figure 16 by the tranverse temperature slices at $7.5R$ intervals. At an axial distance of $7.5R$ the jet shows relatively high-order small-scale surface fluting similar to the previous dynamical times. At larger axial distance the transverse structure is dominated by much larger scale distortion. At axial distances $22.5R$

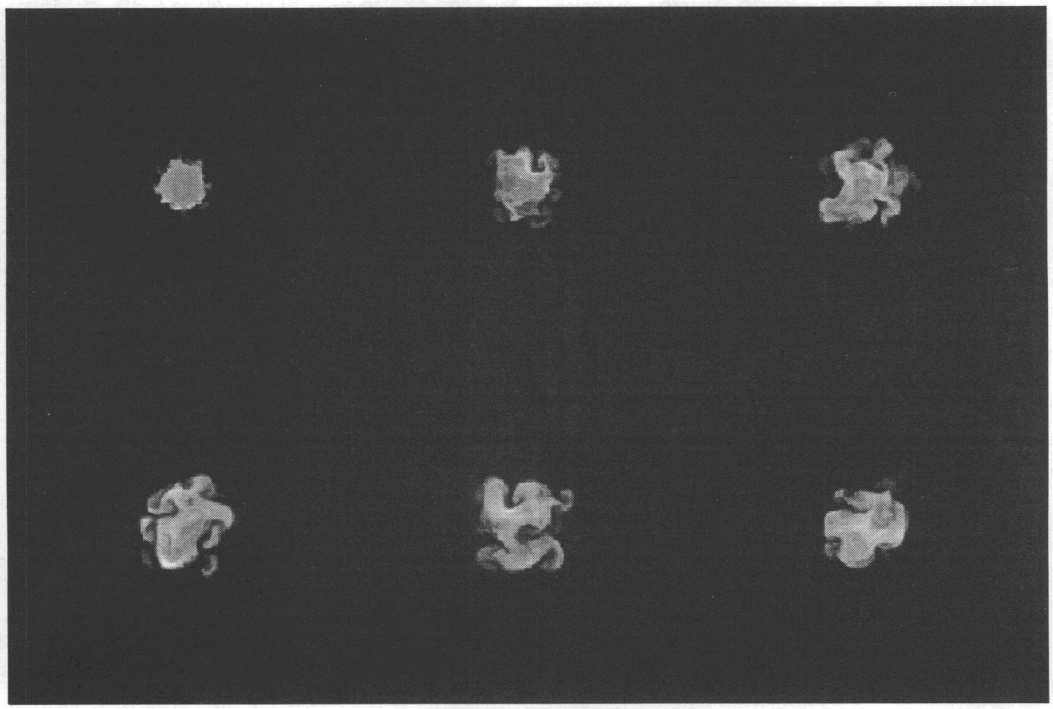

FIG. 10.—Gray-scale rendering of the temperature on two-dimensional planes orthogonal to the jet axis at distances from 7.5 to 45 jet radii in increments of 7.5 jet radii, from top left to bottom right, at time $\tau = 6$. Lighter gray indicates higher temperature.

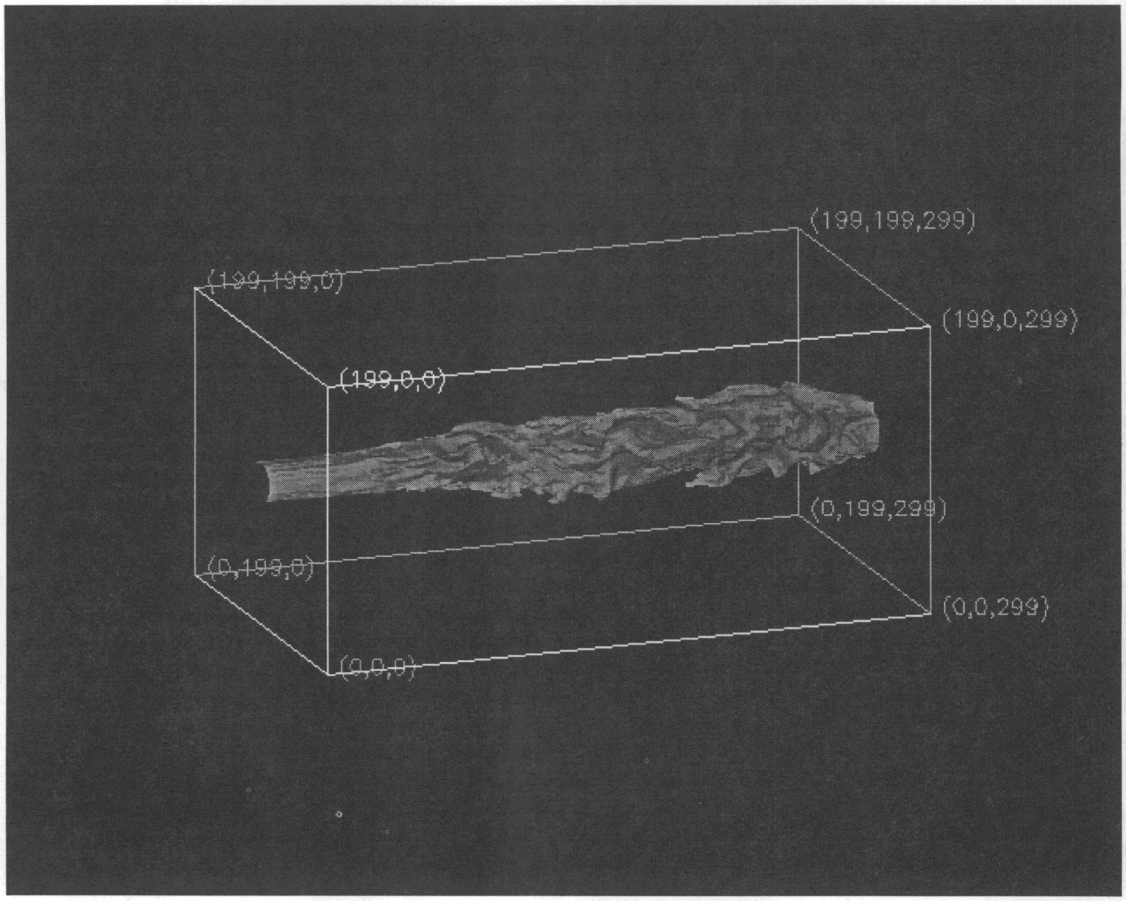

FIG. 11*a*

FIG. 11.—Isotemperature surfaces, (*a*) inside the jet revealing the helical distortion and (*b*) separating the hotter jet and entrained material from the cooler external material at time $\tau = 6$.

jet flattening is evident, and at $37.5R$ the jet breaks up into filaments. The transverse temperature slices also reveal the increasingly chaotic nature of the jet at larger axial distance and, like the axial temperature slices, suggest significant mixing of jet and external material. It is also clear that the initial highly collimated flow is rapidly expanding. This expansion is shown most graphically by the isotemperature surface shown in Figure 17. Collimation begins to break down at axial distances beyond $15R$ as large-scale surface distortion becomes important, and this image, along with the transverse temperature slices, suggests a turbulent mass-entraining expanding jet. Animation shows that a quasi-steady state has nearly been achieved by this dynamical time, with only small transverse expansion still occurring at the largest axial distances. At $45R$ the initial collimated flow has expanded by about a factor of 3. Two orthogonal line-of-sight integrations, *not along the* 2- *and* 3-*axes*, of the velocity divergence shown in Figure 18 reveal that compressions are not simple filaments of circular cross section; e.g., the bright filament at $15R$ Figure 15*b* is not clearly visible in Figure 15*a*. However, animation of line-of-sight images about the axis shows that features tend to wrap around the jet surface. This implies that features have ribbon-like structure that twists about the jet. Animation of images also shows that the jet has developed a helical twist and line-of-sight integrations along the 2-axes of temperature and velocity shear (Fig. 19) reveal that a helical structure of wavelength $\sim 23R$ exists inside the jet.

2.5. *Summary*

At the earliest times, $\tau \leq 3$, the simulation shows symmetric pinching and asymmetric purely sinusoidal distortion. Pinching and sinusoidal distortion occur with wavelength on the order of 5 and 10 times the jet radius, respectively, and produce relatively large-amplitude velocity fluctuations. The largest-effect is associated with pinching distortions, and the accompanying velocity fluctuation along the jet axis produced by nearly conical shocks shows an exponential decline of the minimum velocity from $\sim 15a_x$ at axial distance $\sim 20R$ to $\sim 7a_x$ at $\sim 30R$. The typical fluctuation is on the order to the jet sound speed ($a_j \sim 3a_x$). The sinusoidal distortion produces fluctuation in the transverse velocity along the jet axis on the order of one-third the jet sound speed, and a short-wavelength ($\sim 5R$) oscillation in the transverse velocity along the jet axis is no more than one-tenth of the jet sound speed. However, at later times, $\tau \geq 6$, pinching and the accompanying conical shocks have almost disappeared, and helical and elliptical distortions dominate jet dynamics on the largest scales with a characteristic wavelength of ~ 21 and ~ 12 jet radii, respectively. The short-wavelength oscillation in the transverse velocity along the jet axis seen at early times has grown to about

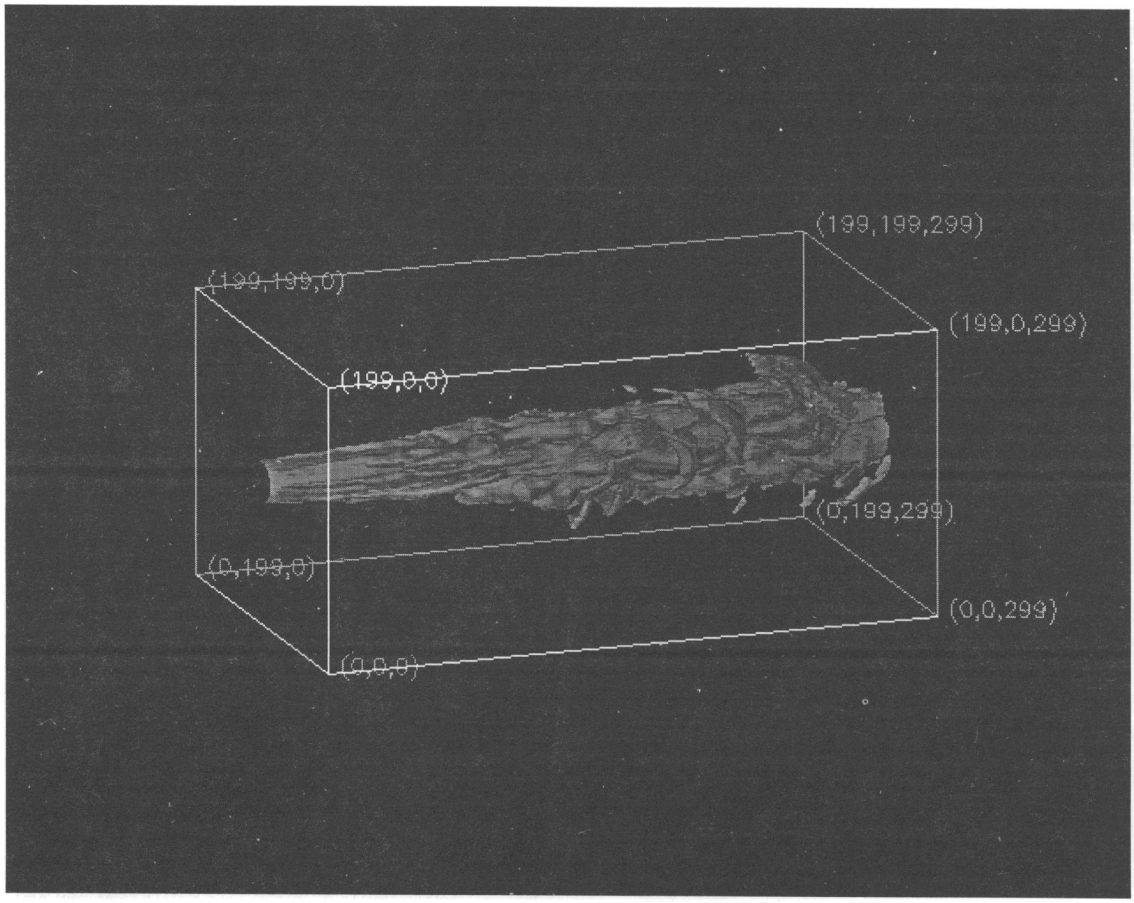

FIG. 11*b*

two-thirds of the jet sound speed. The long-wavelength oscillation in the transverse velocity is only about one-third of the jet sound speed. At the end of the simulation the velocity and Mach number remain relatively constant out to an axial distance of $\sim 25R$. Beyond $25R$ the jet heats, expands, and entrains external material, and at larger distance the velocity and Mach number decline to about one-half the initial values. At the end of the simulation the isotemperature surface separating hot jet and entrained material from the cooler external medium suggests a plumelike morphology, but considerable organized structure is evident in the line-of-sight images internal to the isotemperature surface.

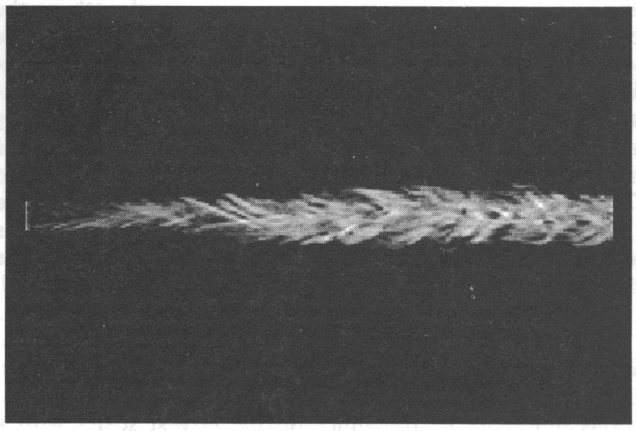

FIG. 12*a*

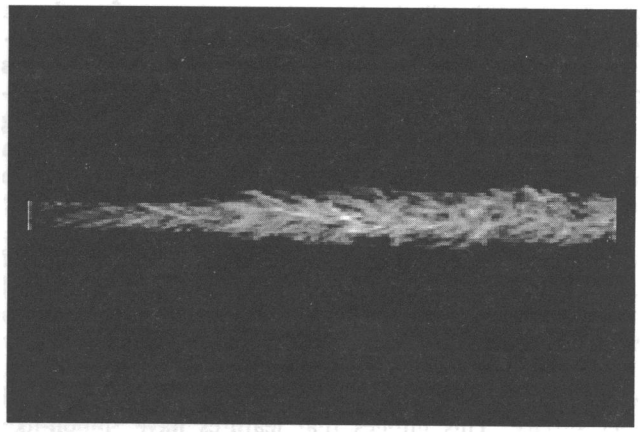

FIG. 12*b*

FIG. 12.—Ray integrations along orthogonal axes (*not the* 2- *and* 3-*axes*) of the velocity divergence (indicates the location of shocks) through the data cube at time $\tau = 6$.

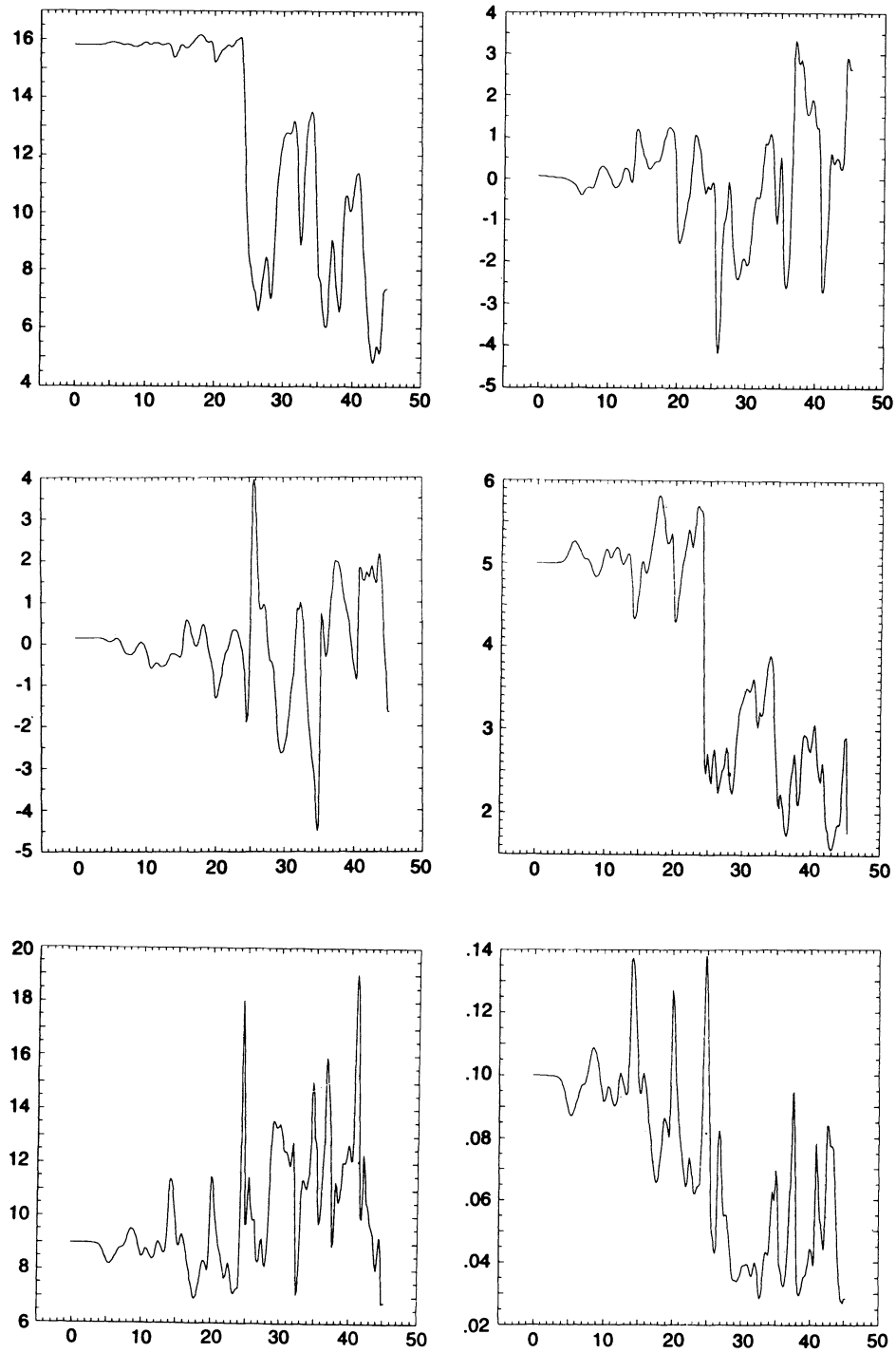

FIG. 13.—Axial 1-velocity (*top left*), transverse 2-velocity (*top right*) and 3-velocity (*middle left*), Mach number (*middle right*), temperature (*bottom left*), and density (*bottom right*) along the jet axis at time $\tau = 12$. Velocities are scaled relative to the sound speed in the medium external to the jet, and the axial distance is scaled relative to the jet radius. Density and temperature units are arbitrary and should be judged relative to their values at the origin.

3. STABILITY AND COLLIMATION OF THE FLOW

3.1. *Normal Modes of the Cylindrical Jet*

Previous work suggests that many of the features seen in the simulations will correspond to structures predicted to arise from Kelvin-Helmholtz instability of the flow. Structures produced by Kelvin-Helmholtz instability can be found from the dispersion relation obtained by linearizing the time-dependent fluid equations for an equilibrium fluid jet, e.g., Hardee & Clarke (1992). The dispersion relation describes the propagation and growth or damping of the Fourier components comprising perturbations to a cylindrical jet. The Kelvin-Helmholtz normal modes are of the form $f(r, \phi, z) = g_n(r) \exp i(kz \pm n\phi - \omega t)$ and consist of surface modes and

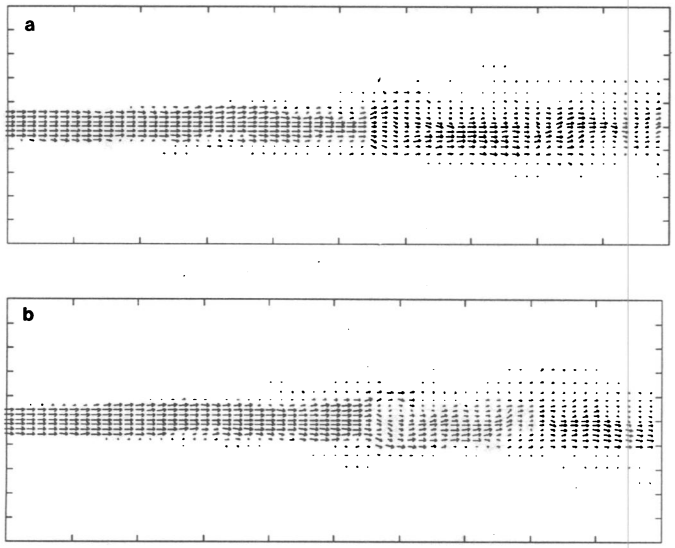

FIG. 14.—Vector velocities on the orthogonal planes through the jet axis at time $\tau = 12$, (*a*) in the (1-axis, 2-axis)-plane and (*b*) in the (1-axis, 3-axis)-plane.

associated body modes. The normal mode with $n = 0$ has no azimuthal dependence, corresponds to pinching of the jet, and will not be considered further here. The normal modes with $|n| \geq 1$ describe helical ($n = 1$), elliptical ($n = 2$), triangular ($n = 3$), square ($n = 4$), and pentagonal ($n = 5$) distortions of the jet, and all distortions twist helically along the jet. The radial dependence, $g_n(r)$, depends on the mode number n and on whether a surface or associated body mode is being described.

In the simulation the jet is perturbed at the origin by a purely real frequency, ω, and thus at long times the stability of the flow is expected to be described by a complex wavenumber, k. The imaginary part of the wavenumber, $k_i = l_i^{-1}$, specifies an inverse growth (or damping) length over which amplitudes grow (or damp) by a factor e. The higher order modes, $n > 1$, can be thought of as higher order harmonics of the helical mode. If, for example, the helical mode is considered to be represented by a single wave front helically twisted along the jet, then the elliptical mode is represented by two wave fronts helically twisted along the jet but separated by 180° in azimuth. The real part of the wavenumber, k_r, provides the wavelength, λ, along z (axial direction), which, for example, represents a sinusoidal oscillation in the displacement of the cylindrical jet surface at fixed azimuth ϕ_s. The length in the z-direction over which a wave front associated with a normal mode n twists 360° around the jet circumference will be given by $l_{rn} \equiv n\lambda_n = 2\pi n/k_{rn}$. Solutions to the dispersion relation for the first five surface modes, $n = 1, 2, 3, 4, 5$, and for the first three body modes associated with surface modes $n = 1, 2, 3$, are shown in Figure 20 for parameters appropriate to the numerical simulation, i.e., $M_j = 5$, $M_x = 15.8$. The solid vertical line in the figure indicates the location of the driving frequency used in the numerical simulation. On a supersonic jet there is a maximum in the imaginary part of the wavenumber, k_{in}^*, corresponding to a minimum growth length, l_{in}^*, and fastest spatial growth rate at a resonant frequency and wavelength ω_n^* and $\lambda_n^* = 2\pi/k_{rn}^*$, respectively. Provided that $M_j \gg 1$ and $M_x \gg 1$, the surface modes have a maximum spatial growth rate at frequency, wavelength, and phase speed that are approximately given by (Hardee 1987)

$$\frac{\omega_n^{s*} R}{a_x} \approx \left(n + \frac{1}{2}\right)\frac{\pi}{4},$$

$$\frac{\lambda_n^{s*}}{R} \approx \frac{8}{n + 1/2}\frac{M_j M_x}{M_j + M_x},$$

$$\frac{v_{\rm ph}^{s*}}{u} \approx \frac{M_j}{M_j + M_x},$$

and have a growth length

$$\frac{l_{in}^{s*}}{R} \approx \frac{M_j}{n}$$

over which the amplitude grows by a factor e. Note that equations (2) and (3) in Hardee & Clarke (1992) for the resonant frequencies and wavelengths of the surface modes were based on analytically determined forms for the resonant frequency and wavelength given by Hardee (1987). In Hardee (1987) more exact empirically determined forms were also obtained, and approximations to those expressions are shown above. The present expressions can be obtained from equations (2) and (3) in Hardee & Clarke (1992) by replacing the factor $(n + \frac{1}{2})\pi/2$ in equation (2) for the resonant frequency with $(n + \frac{1}{2})\pi/4$ and by replacing the factor $4/(n + \frac{1}{2})$ in equation (3) for the resonant wavelength with the factor $8/(n + \frac{1}{2})$. The driving frequency in the numerical simulation was chosen to be near the resonant frequency of the helical surface mode. The resonant frequency increases as the mode number increases and the associated resonant wavelength decreases. At frequencies much below ω_n^{s*} the surface mode solutions to the dispersion relation consist of a growing and damped pair with

$$\frac{ku}{\omega} \approx 1 \mp i\eta^{1/2},$$

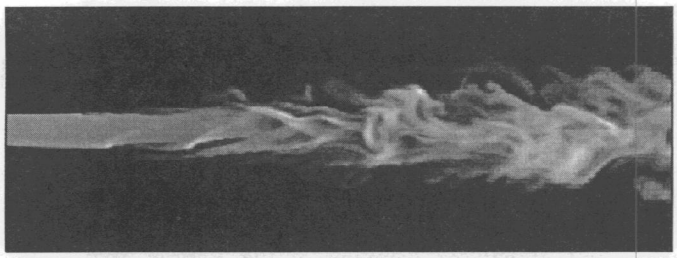

FIG. 15*a*

FIG. 15*b*

FIG. 15.—Gray-scale rendering of the temperature on orthogonal planes through the jet axis at time $\tau = 12$, (*a*) in the (1-axis, 2-axis)-plane and (*b*) in the (1-axis, 3-axis)-plane, corresponding to the vector velocities shown in Fig. 14. Lighter gray indicates higher temperature.

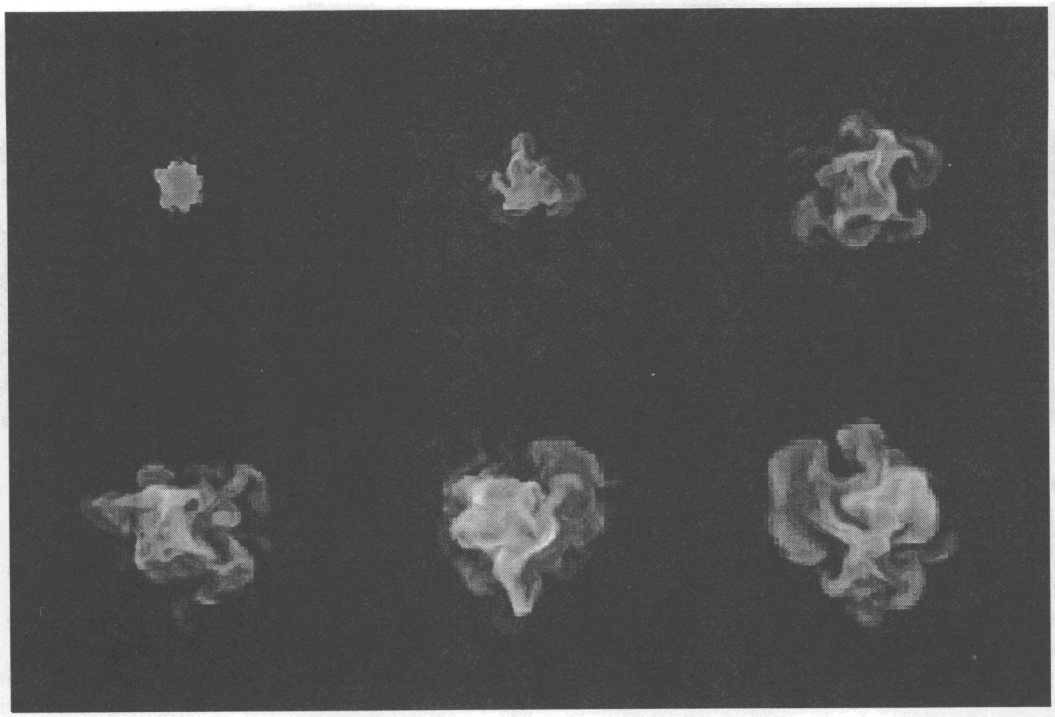

FIG. 16.—Gray-scale rendering of the temperature on two-dimensional planes orthogonal to the jet axis at distances from 7.5 to 45 jet radii in increments of 7.5 jet radii, from top left to bottom right, at time $\tau = 12$. Lighter gray indicates higher temperature.

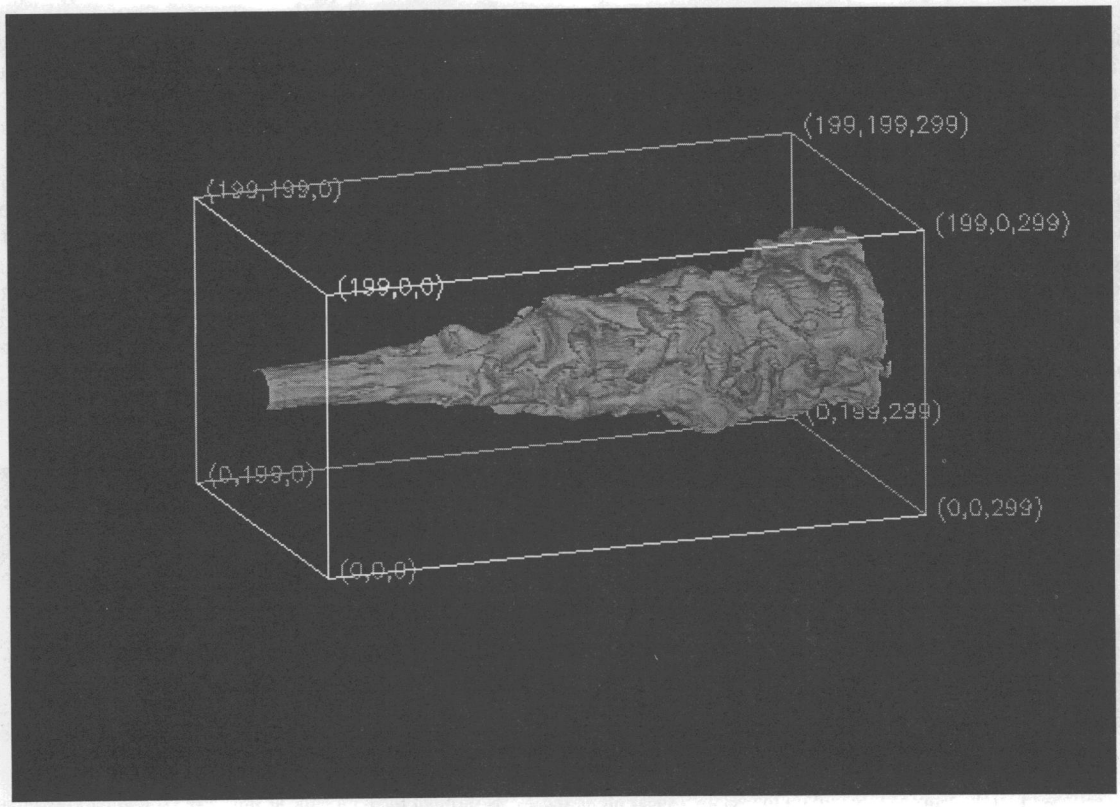

FIG. 17.—Isotemperature surface separating the hotter jet and entrained material from the cooler external material at time $\tau = 12$.

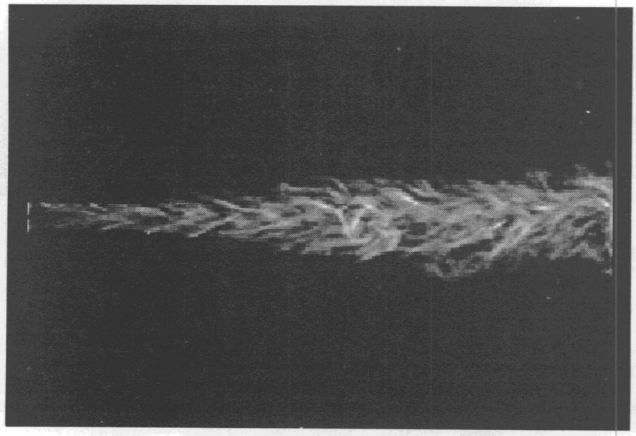

FIG. 18a

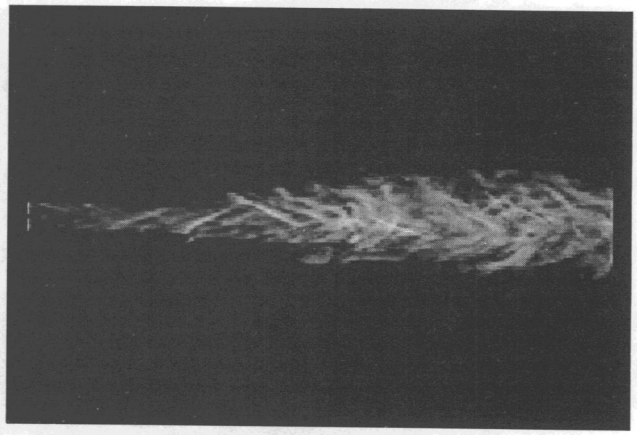

FIG. 18b

FIG. 18.—Ray integrations of the velocity divergence (indicates the location of shocks) along orthogonal axes (*not the* 2- *and* 3-*axes*) through the data cube at time $\tau = 12$.

where $\eta \equiv \rho_j/\rho_x = (M_j/M_x)^{1/2}$ is the ratio of jet density to external density for a pressure-matched jet and external medium. At frequencies much above ω_n^{s*} the surface mode changes character, and the real parts of the solutions are given by

$$\frac{ku}{\omega} \approx \frac{u}{u \mp a_j} .$$

These solutions are easily identified as sound waves moving forward and backward with respect to the jet fluid, although since the jet is supersonic all waves move forward with respect to the external medium. In the frame of the jet fluid, backward-moving waves are growing and forward-moving waves are damped. Numerical simulations have shown that these high-frequency waves are not destructive to the jet, and that for the sinusoidal mode on a slab jet which is analogous to the helical mode on a cylindrical jet this change in character occurs when $\omega > 1.5\omega^*$ (Hardee, Cooper, & Clarke 1994). Similarity between the sinusoidal oscillation of a slab jet and the helical twisting of a cylindrical jet implies that this relation holds true for the helical mode. Note that this change in character also occurs for the higher order surface modes, but the frequency at which this change in character occurs cannot be extracted from previous two-dimensional simulations because the higher order surface modes do not have a two-dimensional analog.

The stability of a system can also be analyzed by assuming that a perturbation is described by Fourier components with a purely real wavenumber. In this case normal mode solutions to the dispersion relation have a complex frequency. The imaginary part of the frequency then specifies an inverse growth time, i.e., $\omega_i = \tau^{-1}$. This approach most properly describes a system on which a wavelength is imposed with initial amplitude uniform in space and whose amplitude subsequently grows in time everywhere at the same rate. For example, a numerical simulation of jet stability initialized using periodic boundary conditions should evolve as described by the temporal development of the initial perturbation wavelength. Interestingly, previous light ($\eta \ll 1$) equilibrium slab jet simulations suggested that the initial behavior of the jet was most accurately described by the development of rapidly growing sinusoidal oscillations at wavelengths corresponding to the maximum growth rate and not the driving frequency. It was ascertained that the initial perturbation was produced by a pressure pulse moving down the jet at speed $u + a_{in}$ relative to the ambient medium, whereas information about the perturbing frequency was conveyed down the jet at speed $\sim[\eta^{1/2}/(1 + \eta^{1/2})]u = [M_j/(M_j + M_x)]u$, which on a light supersonic jet is much less than $u + a_{in}$. This initial perturbation led to the development of a growing sinusoidal oscillation essentially in situ which subsequently destroyed continuous flow (Hardee et al. 1991; Zhao et al. 1992a, b). This behavior is similar to temporal growth of an initially imposed wavelength, and for this reason we show the solution to the dispersion relation describing temporal growth of the helical surface mode in Figure 21. Note that the real part of the wavenumber for the helical surface

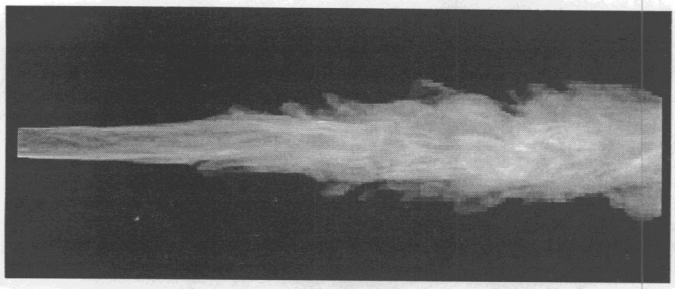

FIG. 19a

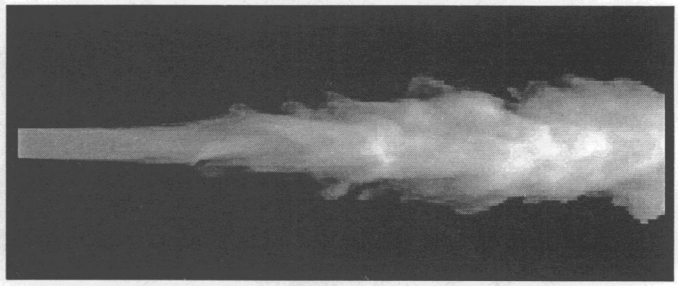

FIG. 19b

FIG. 19.—Ray integrations of (*a*) the temperature and (*b*) the velocity shear along the 2-axis through the data cube at time $\tau = 12$. Lighter gray indicates hotter material or higher shear, and shear surfaces show up as lines in this image.

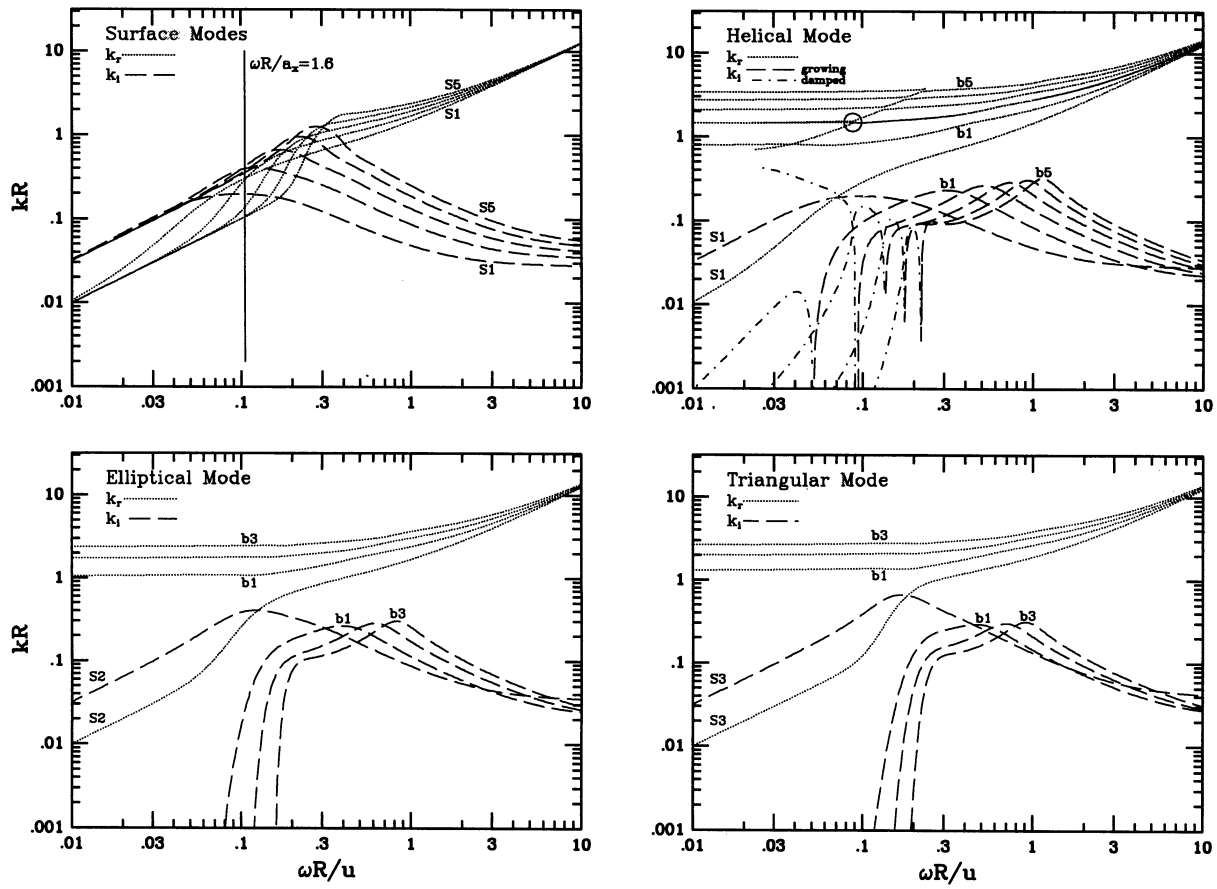

FIG. 20.—Numerical solution of the dispersion relation for potentially important surface and body modes. The real part of the wavenumber is shown by the dotted lines, and the imaginary part of the wavenumber for growing (damped) perturbations is shown by the dashed (dash-dot) lines. The precession frequency used in the simulation is indicated by the solid vertical line.

mode at the fastest spatial growth rate (Fig. 20) and the wavenumber at the fastest temporal growth rate (Fig. 21) are significantly different, and we will find that the initial behavior of the three-dimensional simulation is best described by the fastest temporally growing helical mode.

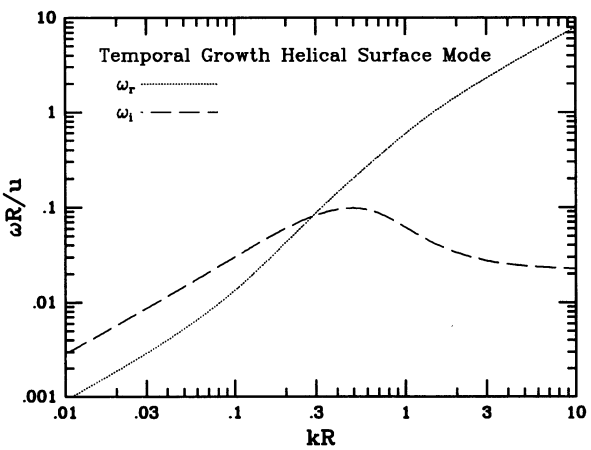

FIG. 21.—Numerical solution of the dispersion relation for the surface helical mode assuming a purely real wavenumber. The real part of the frequency is shown by the dotted line, and the imaginary part of the frequency for a growing perturbation is shown by the dashed line.

If only undamped solutions are shown, then the structure of the normal body mode solutions associated with the normal surface modes is relatively simple, as is shown for the elliptical and triangular modes. Like the surface mode, the body modes exhibit a maximum spatial growth rate at some resonant frequency. Higher order body modes have a maximum spatial growth rate at a higher resonant frequency with the maximum growth rate increasing logarithmically with the resonant frequency (Hardee 1987; Payne & Cohn 1985). At higher frequencies solutions consist of forward-moving damped and backward-moving growing sound waves (in the jet fluid frame) mathematically identical to the high-frequency surface modes. Note that at any fixed frequency one of the surface modes always grows more rapidly than the body modes. For the $n = 1$ helical mode, the body modes have somewhat higher maximum growth rates than the surface mode, but all other surface modes grow faster than the accompanying body modes. At low frequencies the actual solution structure of the body modes is more complicated and is shown in detail only for the helical mode. Even here the exact structure was only examined within and in a region around the circle on Figure 20. In general, at the lower frequencies the body modes are revealed to consist of a damped solution, $k_i > 0$, in addition to a purely real solution, $k_i = 0$, where the purely real solution has a slightly larger real wavenumber. The practical consequence of this result is that there should be no low-frequency and large-scale structure internal to the jet surface associated

with the body modes, as solutions are either purely real or strongly damped and phase velocities approach zero.

3.2. *Jet Distortion Produced by Surface and Body Modes*

The pressure, radial velocity, and radial displacement perturbations associated with the normal modes are given in (e.g., Birkinshaw 1991; Hardee 1983)

$$P^1(r) = P_s^1 \frac{J_n(\beta r)}{J_n(\beta R)} \exp\left[i(kz \pm n\phi_s - \omega t)\right],$$

$$v_r^1(r) = v_{rs}^1 \frac{J_n'(\beta r)}{J_n'(\beta R)} \exp\left[i(kz \pm n\phi_s - \omega t)\right],$$

$$\xi_r^1(r) = \xi_{rs}^1 \frac{J_n'(\beta r)}{J_n'(\beta R)} \exp\left[i(kz \pm n\phi_s - \omega t)\right],$$

where P_s^1, v_{rs}^1 and ξ_{rs}^1 are the surface amplitudes of the pressure, the radial velocity, and the radial displacement perturbations. Note that $\partial\xi_r^1/\partial t = v_r^1$ and therefore $\xi_r^1(r) \propto v_r^1(r)/\omega$. The primes on the Bessel functions denote derivatives with respect to the arguments, and $\beta = F(\omega, k)$ where ω and k are normal mode solutions of the dispersion relation. The dependence of the radial fluid displacement as a function of radius inside the jet surface, $\xi_r^1(r) \propto J_n'(\beta r)/J_n'(\beta R)$, of a surface mode can be shown analytically to be approximately given by $\xi_r^1(r) \propto (r/R)^{n-1}$, where n is the mode number (Hardee 1983). Thus, the helical mode ($n = 1$) is expected to have little or no dependence on radius and moves the entire jet, whereas significant displacement associated with the higher order surface modes is confined to be near the jet surface.

Numerical solution of $J_n'(\beta r)/J_n'(\beta R)$ and of $J_n(\beta r)/J_n(\beta R)$ for a normal mode gives a complex value for the dependence on radius internal to the jet surface, and the pressure, radial velocity, and radial displacement perturbations associated with the normal modes can be written in the form

$$P^1(r) = A(r)e^{i\phi(r)}P_s^1 \exp\left[i(kz \pm n\phi_s - \omega t)\right],$$

$$v_r^1(r) = A'(r)e^{i\phi'(r)}v_{rs}^1 \exp\left[i(kz \pm n\phi_s - \omega t)\right],$$

$$\xi_r^1(r) = A'(r)e^{i\phi'(r)}\xi_{rs}^1 \exp\left[i(kz \pm n\phi_s - \omega t)\right],$$

where

$$A(r)e^{i\phi(r)} = \left|\frac{J_n(\beta r)}{J_n(\beta R)}\right| \times \exp\left[\left[i \tan^{-1}\left\{\mathrm{Im}\left[\frac{J_n(\beta r)}{J_n(\beta R)}\right] \Big/ \mathrm{Re}\left[\frac{J_n(\beta r)}{J_n(\beta R)}\right]\right\}\right]$$

and

$$A'(r)e^{i\phi'(r)} = \left|\frac{J_n'(\beta r)}{J_n'(\beta R)}\right| \times \exp\left[\left[i \tan^{-1}\left\{\mathrm{Im}\left[\frac{J_n'(\beta r)}{J_n'(\beta R)}\right] \Big/ \mathrm{Re}\left[\frac{J_n'(\beta r)}{J_n'(\beta R)}\right]\right\}\right].$$

Written in this form, it is apparent that there is both an amplitude and an azimuthal phase angle dependence with radius of the perturbation internal to the jet surface relative to the perturbation at the jet surface. The displacement associated with the normal modes relative to the surface displacement and the azimuthal phase angle relative to the phase angle at the surface has been computed at the resonant frequency for helical, elliptical, and triangular surface and first body modes and is shown in Figure 22. The surface modes show a somewhat faster falloff in amplitude relative to the surface amplitude than that predicted by the analytical approximation and significant rotation in aximuth of, say, the maximum internal displacement relative to the maximum surface displacement. Over the interior of the jet likely to be significantly affected by a surface mode, the rotation in azimuth is typically on the order of 30°. The first body modes reveal an interior local minimum coincident with very rapid change in the azimuth. Only the first helical body mode has nonzero displacement at the jet center. At the local minimum where the azimuth is changing rapidly with radius, one would not expect large displacement amplitudes to develop. Thus, the first body modes might affect a region to a depth of $\sim 0.2R$ interior to the jet surface and an inner 20%–25% of the jet where the displacement is shifted in azimuth by $\sim 220°$ relative to the surface displacement. A cut along a radius at constant azimuth, say, $\phi - \phi_s = 0$ (Fig. 23), shows a decline in displacement of the surface modes slightly faster than that shown in Figure 22 as a result of the rotation in azimuth of the maximum internal displacement relative to the maximum surface displacement. The body modes show a reversal in fluid displacement at a null surface which occurs at the radius at which $\phi - \phi_s = 90°$ in Figure 22.

The behavior of the fluid displacement associated with the surface and the first body helical, elliptical, and triangular modes is illustrated in Figure 24. In the figure the outer contour illustrates the surface distortion caused by either a surface mode or the first body mode. The inner contour illustrates the inner distortion caused by the first body mode at the radius where $\phi - \phi_s = 180°$. For example, the first helical body mode deforms an inner portion of the jet into a helical twist with displacement approximately opposed to the displacement of the jet surface associated with the mode. In Figures 22 and 23 the displacement is normalized relative to the surface displacement. Note, however, that the maximum surface displacement at the maximum growth rate is a function of the mode because $\xi_r^1(r) \propto v_r^1(r)/\omega^*$. Because motions in the radial direction are not likely to exceed the jet sound speed, i.e., $v_r^1(r) \leq a_j$, and ω^* increases with n and also increases for higher order body modes, the largest amplitudes should be associated with the lowest order surface modes and the accompanying lowest order body modes.

3.3. *Comparison of Stability Theory and Simulation*

In a previous Mach 3 simulation the helical and elliptical surface modes were indentified and compared with predictions made by the stability theory (Hardee & Clarke 1992). Table 1 contains wavelengths and length scales observed in the previous Mach 3 simulation and in the present Mach 5 simulation along with the wavelengths and length scales predicted by the theory that appear to correspond to observed features in the numerical simulations. Note that the initial development of sideways oscillation in the Mach 5 simulation appears best described by temporal growth of the helical mode at a wavelength near to the fastest temporal growth. Additionally, we observe that this initial growth is of a sinusoidal and not a helical nature. This observation confirms that information about precession at the origin is communicated down the light jet much more slowly than the initial perturbation which we identify with a fast-moving pressure pulse. This result also confirms that opposed helical twists grow equally in the absence of significant jet rotation or magnetic field helicity, i.e., the sinu-

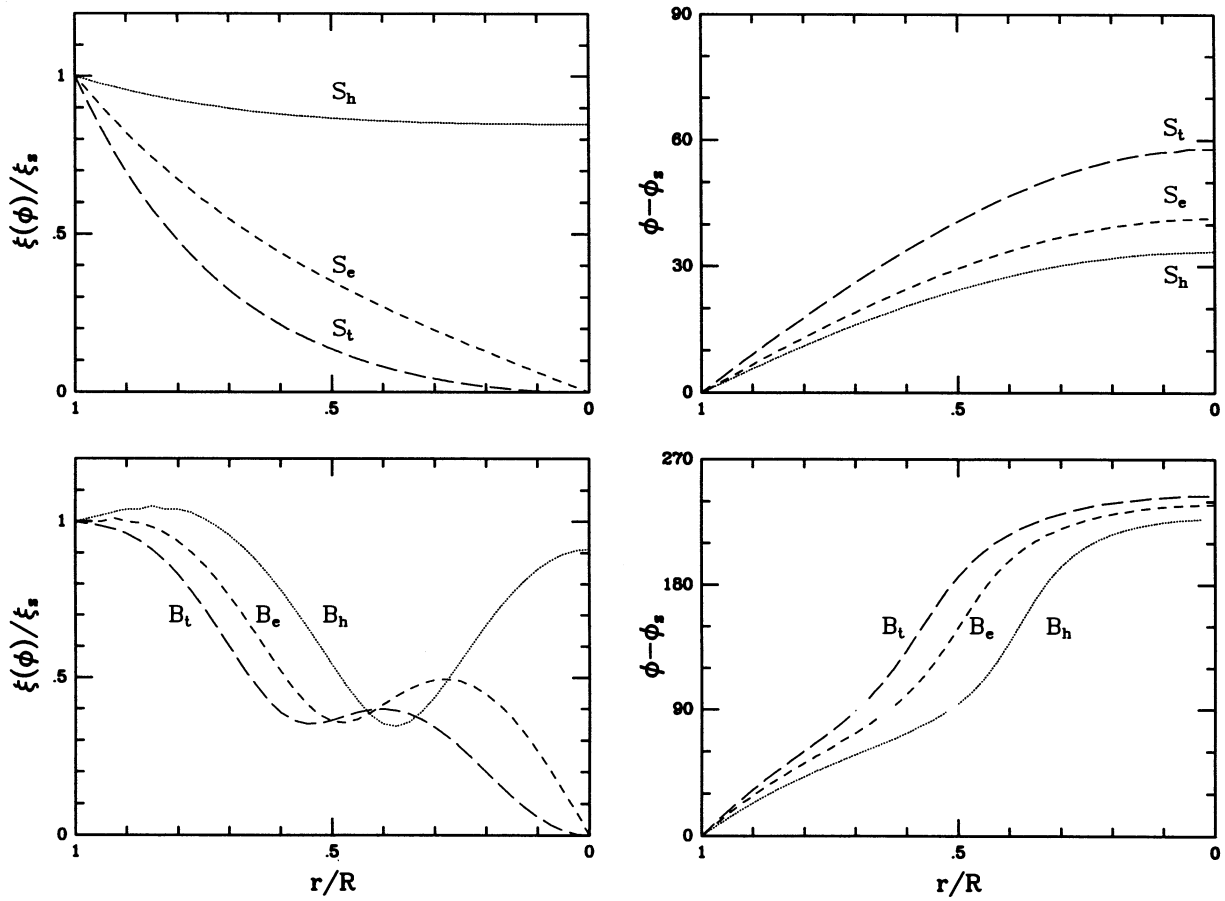

FIG. 22.—Amplitude ξ and phase angle $\phi - \phi_s$ relative to the displacement ξ_s at the jet surface as a function of radius for helical, elliptical, and triangular surface (S) and first helical, elliptical, and triangular body (B) modes.

soidal oscillation can be thought of as the superposition of left and right circularly polarized helical waves of equal amplitude.

At later times the observed helical wavelength in the Mach 3 and Mach 5 simulations is in good agreement with that predicted by the linear theory to correspond to the driving frequency. In the Mach 3 simulation the elliptical wavelength appears to be about half the helical wavelength; this is about 50% longer than the wavelength corresponding to maximum elliptical growth but over a factor of 3 shorter than the elliptical mode wavelength associated with the driving frequency. The elliptical wavelength can be understood if the wave fronts associated with the elliptical mode wind around the jet with about the same helical pitch as the wave front associated with the helical mode, i.e., $\lambda_1^s \approx l_{r2} = 2\lambda_2^s$. This result suggests a nonlinear coupling between the wave fronts describing these normal modes. Recall that the two wave fronts associated with

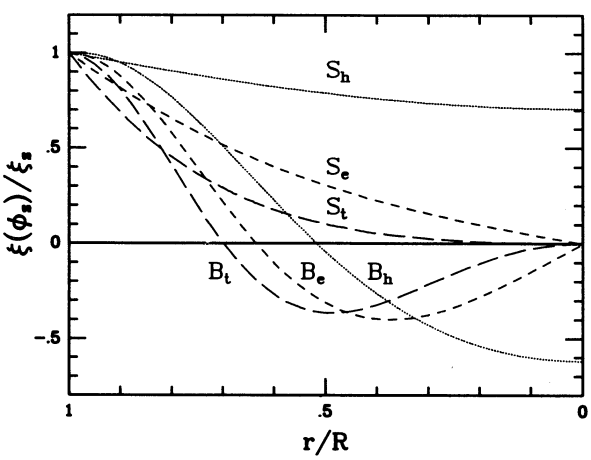

FIG. 23.—Displacement amplitude ξ as a function of radius relative to the displacement at the jet surface at constant phase angle $\phi = \phi_s$ for helical, elliptical, and triangular surface (S) and first helical, elliptical, and triangular body (B) modes. The displacement is zero at the radial distance where $\phi - \phi_s = 90°$ in Fig. 22.

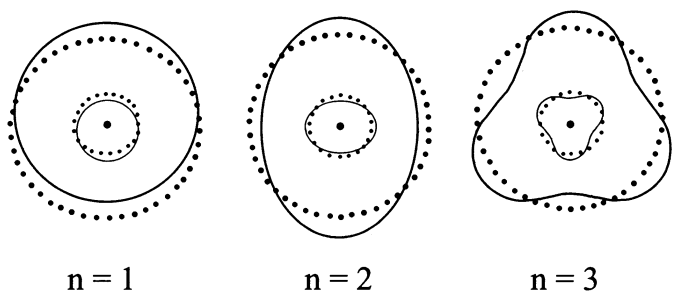

FIG. 24.—Illustration of fluid displacements at the jet surface associated with helical, elliptical, and triangular surface (S) or of fluid displacements at the jet surface and at the internal location where $\phi - \phi_s = 180°$, associated with the first helical, elliptical, and triangular body (B) modes. The undisplaced surfaces are indicated by the dotted circles.

TABLE 1

OBSERVED AND CALCULATED HELICAL SURFACE-BODY AND ELLIPTICAL SURFACE MODES

τ	λ_1^s/R	l_{i1}^s/R	λ_1^{b1}/R	l_{i1}^{b1}/R	λ_2^s/R	l_{i2}^s/R
			Mach 3 Jet Simulation			
≤ 8	~ 10 (10.9[a])	(2.9[a])	...	...	~ 9 (7.9[a])	(1.5[a])
≥ 12	~ 24 (23.7[b])	(3.3[b])	~ 3 (2.9[a])	(2.3[a])	~ 12 (41.9[b])	(2.5[b])
			Mach 5 Jet Simulation			
~ 3	~ 10 (12.8[c])	...	...	...	...	...
~ 6	~ 19 (22.2[a])	(5.1[a])	~ 5 (5.7[a])	(4.3[a])	~ 14 (15.9[a])	(2.5[a])
~ 12	~ 21 (21.7[d])	(5.1[d])	~ 5 (7.4[d])	(10.1[d])	~ 10 (19.3[d])	(2.6[d])

NOTE.—Calculated values are given in parentheses.
[a] Value at maximum spatial growth.
[b] Value at $\omega R/a_x = 1.0$.
[c] Value at maximum temporal growth.
[d] Value at $\omega R/a_x = 1.6$.

the elliptical mode are at opposite ends of a jet diameter and, say, correspond to the major axis of the elliptical distortion. In the Mach 5 simulation the observed helical wavelength $\lambda_1^{obs} \approx 21R$ (average value $\tau > 6$) and is in excellent agreement with the wavelength $\lambda_1^s|_\omega = 21.7R$ predicted by the linear theory to correspond to the driving frequency. The observed elliptical length scale $l_{r2}^{obs} = 2\lambda_2^{obs} \approx 24R$ (average value $\tau > 6$) is significantly less than the predicted length scale at maximum growth, $l_{r2}^* = 2\lambda_2^{s*} = 31.8R$, and much less than the length scale predicted to correspond to the driving frequency, $l_{r2}|_\omega = 2\lambda_2^s|_\omega = 48.6R$. The close agreement between the observed helical wavelength λ_1^{obs} and the observed elliptical length scale l_{r2}^{obs}, within the 10% errors, again suggests a nonlinear coupling between helical and elliptical modes. Thus, we confirm the results obtained in the previous Mach 3 simulation, but now at somewhat higher Mach number and at higher grid resolution. We conclude from this confirmation of the previous results that the longest length scale behavior is satisfactorily resolved and converged at the present grid resolution.

The theory predicts that the helical growth length ($l_{i1}^s \sim 5.1R$) corresponding to the observed helical wavelength ($\lambda_1^{obs} \sim 21R$) in the present Mach 5 simulation will be 1.6 times longer than the helical growth length ($l_{i1}^s \sim 3.3R$) corresponding to the observed wavelength ($\lambda_1^{obs} \sim 24R$) in the previous Mach 3 simulation. The theory predicts that the elliptical growth length ($l_{i2}^s \sim 2.5R$) associated with the observed elliptical wavelength ($\lambda_2^{obs} \sim 12R$) in the present Mach 5 simulation will be 1.7 times longer than the elliptical growth length ($l_{i2}^s \sim 1.5R$) associated with the observed elliptical wavelength ($\lambda_2^{obs} \sim 12R$) in the previous Mach 3 simulation. The theory predicts that the spatial growth length of the helical surface mode is about twice that of the elliptical surface mode, and we find that elliptical distortion develops more rapidly than helical twisting. However, the rapid disruption of highly ordered flow associated with the primarily dual filamentation arising from elliptical distortion allows no direct comparison between helical and elliptical spatial growth rates. Elliptical distortion reaches a maximum in the Mach 3 and Mach 5 simulations at axial distances between $13R$ and $28R$ and between axial distances $18R$ and $30R$, respectively. Abrupt axial velocity decrease varies in location but occurs between $14R$ and $19R$ and $20R$ and $25R$ in the Mach 3 and Mach 5 simulations, respectively. The transverse velocity perturbation applied in the Mach 5 simulation is $\frac{5}{3}$ that applied in the Mach 3 simulation, providing an initial transverse velocity which is a larger fraction of the jet sound speed. This complicates direct comparison between the two simulations. If growth were strictly exponential, the transverse velocity would grow as $v_\perp = v_{\perp 0} e^{z/l}$. The difference in initial amplitude would reduce the number of e-foldings required to reach a given transverse velocity, say the jet sound speed, by about $e^{1/2}$, or about half an e-folding length in the Mach 5 simulation. The distances at which the observed distortions and abrupt velocity decrease occur are about 11 growth lengths ($16.5R$) and about 9 growth lengths ($22.5R$) of the observed elliptical distortion in the Mach 3 and Mach 5 simulations, respectively. By way of comparison, these distances also correspond to about 5 growth lengths and about 4.5 growth lengths of the observed helical twist in the Mach 3 and Mach 5 simulations, respectively. While these results appear consistent with our expectation of slower growth in the Mach 5 simulation, it should be noted that growth of the transverse velocity corresponding to large-scale helical twisting is slower than exponential in both simulations, and in neither simulation does transverse oscillation associated with helical twisting achieve the expected maximum amplitude ($\sim R$) or achieve the expected maximum transverse velocity ($\sim a_j$) (Hardee 1987). Because the appropriate initial amplitude of the elliptical distortion is not known and the velocity structure of the growing elliptical distortion is difficult to probe, we do not know whether elliptical growth is slower than exponential, although this seems likely given the larger number of elliptical growth lengths required to reach the maximum elliptical distortion seen in the simulations.

The short-wavelength, $\lambda^{obs} \sim 5R$, velocity oscillation in the transverse direction along the jet axis has a wavelength only slightly shorter than the fastest spatially growing wavelength ($\lambda_1^{b1*} = 5.7R$) associated with the first helical body mode. Examination of the transverse velocity along the jet axis in the Mach 3 simulation also shows velocity oscillation, but with wavelength $\lambda^{obs} \sim 3R$, and this is approximately the fastest spatially growing wavelength associated with the first helical body mode in the Mach 3 simulation ($\lambda_1^{b1*} = 2.9R$). In the Mach 5 simulation the 2-velocity and 3-velocity oscillations appear to be out of phase by approximately 1 jet radius, and this would be consistent with a helical twist of the inner part of the jet. The short wavelength in the Mach 3 simulation places the phase shift between the 2-velocity and the 3-velocity components corresponding to a helical twist of the inner portion of

the jet at approximately $\frac{1}{2}$ jet radius, and this is too small a shift to be verified. Nevertheless, we feel confident in saying that both simulations show evidence for helical twisting of the jet center predicted by the theory to arise from the first helical body mode. The theory suggests that this twisting will be confined to the inner 20%–25% of the jet. The Mach 3 simulation *was not driven* at the resonant frequency of the helical surface mode, and the Mach 5 simulation *was driven* at the resonant frequency of the helical surface mode, but both simulations showed evidence for the first helical body mode at wavelength near maximum spatial growth. Based on these two simulations, we would conclude that the first helical body mode is not coupled to the surface mode. The first body mode is also predicted to affect the outer 20% or so of the jet. While there is evidence for organized structure at the jet surface at short wavelengths, it is not possible to tell whether this structure is related to the first helical body mode or is related to higher order surface modes.

3.4. *Jet Collimation*

At an axial distance of $\sim 25R$ the jet velocity and Mach number undergo a sudden drop by about a factor of 2 as the result of the development of instability, and the jet becomes effectively transonic with an internal Mach number of ~ 2.5 at axial distances larger than $25R$. In this region the transverse velocities are $\approx a_j$, the jet density has decreased by about a factor of 2, and the jet temperature has risen by about 30% (see Fig. 13). Axial temperature slices along the 2- and 3-axes (Fig. 15) and the isotemperature surface (Fig. 17) reveal that the jet expands by about a factor of 3 between axial distances $15R$ and $45R$. The images and the plots suggest a turbulent mass-entraining flow that is also heated by the surface shocks evident in the velocity divergence images (Figs. 18*a* and 18*b*).Turbulent mass-entraining transonic flows have been studied in the context of laboratory jets. Some summary of the existing experimental and theoretical literature on mass-entraining turbulent laboratory jets and possible application to astrophysical jets can be found in a series of papers by Bicknell (1984, 1986a, b). In particular, the equation relating jet slowdown to the jet expansion rate, to the pressure gradient, and to the dissipation rate (eqn. [5.18] in Bicknell 1984) for a completely thermal jet and external medium can be written as

$$\frac{1}{v_c}\frac{dv_c}{dz} = -\frac{3R^2\,dP/dz + 10PR\,dR/dz}{5PR^2 + 4\beta^2},$$

where $v_c(z)$ is the jet velocity on the axis, $R(z)$ and $P(z)$ are jet radius and pressure (pressure balance with the external medium is assumed), and β^2 is the dissipation rate. It follows that

$$v_c \propto P^{-3/(5+4\beta^2/PR^2)} R^{-10/(5+4\beta^2/PR^2)},$$

and dissipation is unimportant for $4\beta^2/PR^2 \ll 5$. If dissipation were entirely due to subsonic turbulence, then $\beta^2 \approx 0.03\pi R^2 \rho_c v_c^2$ (see Bicknell 1984) is the turbulent dissipation rate (heat generation by dissipation and work on turbulent fluctuations). In the simulation, $\rho_c = \rho_{0.1} \equiv 0.1$, $v_c = v_5 \equiv 5$, $T_c \equiv T_9$, and $P = P_{0.6} \equiv 0.6$ represent the initial conditions and provide a reasonable estimate of conditions upstream of axial distance $25R$ at the end of the simulation, and $\rho_c \approx 0.5\rho_{0.1}$, $v_c \approx 0.5v_5$, $T_c \approx 1.3T_9$, and $P \approx 0.65P_{0.6}$ provide a reasonable estimate of conditions downstream of axial distance $25R$ at the end of the simulation. Note that this static thermal pressure downstream of $25R$ is less than the static pressure in the atmosphere and suggests that a significant sideways ram pressure, possibly as much as one-third of the total jet pressure, is supplied by transverse motions associated with the disrupted flow. If transverse motions were subsonic and if dissipation were due entirely to subsonic turbulence, we would predict that $1.7 > 4\beta^2/PR^2 \approx 1.7(\rho_c/\rho_{0.1})(v_c/v_5)^2/(P/P_{0.6}) > 0.3$, and if $4\beta^2/PR^2 \approx 1$, then $v_c \propto P^{-3/6} R^{-10/6}$. In this case we would have expected a decrease in the axial velocity by about a factor of 5 to accompany a tripling in the radius, and this is not the case. However, because transverse velocities are on the order of the jet sound speed, typically 2–3 three times the sound speed in the external medium, and we have found considerable evidence for shocks, it might be expected that a considerably higher dissipation rate is appropriate to the jet. The actual slowdown observed is by about a factor of 2.7, and this implies that $4\beta^2/PR^2 \approx 5$. Thus, from this single numerical experiment we suggest that $\beta^2 \approx 0.15\pi R^2 \rho_c v_c^2$ is more representative of a total dissipation rate in the presence of transonic turbulence and accompanying weak shocks.

4. DISCUSSION

Both the lower resolution Mach 3 simulation and the higher resolution Mach 5 simulation appear to give the same qualitative large-scale features. Comparison with stability theory indicates that the large-scale features are reproduced correctly in a quantitative sense as well. Based on our present results, we would conclude that large-scale features such as helical twisting, elliptical distortion and bifuraction of jet flow, or triangular distortion and trifurcation of jet flow are satisfactorily resolved and converged with 20 zones across a jet diameter. However, the second simulation, with 30 zones across the jet diameter, does show smaller scale features, and there is a qualitative suggestion that the higher resolution used in the second simulation enhances mixing at the jet boundary and the jet spreads somewhat more rapidly. This conclusion must remain tentative in the absence of comparisons among identical simulations with different effective grid resolutions, in particular because the higher Mach number jet associated with the higher resolution simulation carries considerably more energy and the effect of shock heating in a mixing layer will be more profound.

Comparison between simulations and stability theory has shown remarkable quantitative agreement. The two simulations performed to date which used different precession frequencies and jet speeds show that a jet responds to precession with the helical twist predicted by the theory. Both simulations have revealed the importance of the elliptical mode. The elliptical mode ultimately leads to a bifurcation of the flow, and in the present simulations this bifurcation leads to a sudden initial decrease in jet speed along the axis and a subsequent slower decline in outward flow. Bifurcation or occasionally observed trifurcation of the flow is accompanied by mass entrainment, shock heating, and expansion of the initially highly collimated flow, and the initial supersonic flow becomes transonic. In the present simulations the elliptical distortion is twisted and coupled to the helical twist induced by precession at the origin. This coupling is made manifest by the long axis of the elliptical distortion, which rotates through 360° with a wavelength that is similar to the helical wavelength and not, for example, the longer wavelength that would correspond to the fastest spatial growth of the elliptical mode. We note that this might not be the case if a jet were randomly perturbed. In both simulations we observe that the higher order fluting

modes develop on shorter spatial scales, do not significantly decollimate the jet, and are overwhelmed at larger spatial scales primarily by the lower order elliptical and triangular modes. This observation is fully consistent with the theory, which predicts both smaller surface displacements and reduced effect on the jet away from the jet surface for higher order modes.

The theoretically predicted jet distortions induced by surface and body modes were investigated in detail, and the simulations have revealed the presence of a transverse velocity oscillation on the jet axis which we have identified with the first helical body mode. This helical body mode leads to a helical twist of the inner 20%–25% of the jet with a theoretically predicted fastest growing wavelength $\approx$20%–25% of the theoretically predicted fastest growing wavelength of the surface helical mode. In the simulations the first helical body mode does not appear to be coupled to the surface helical mode and appears at the fastest spatially growing wavelength predicted by the theory. Theoretical investigation of the structure and dynamical effect of the body modes reveals that all body modes can be described in terms of a surface displacement which both decreases in amplitude and is rotated in azimuth as a function of distance from the jet surface. Higher order helical body modes associated with higher order fluting modes are predicted to achieve lesser surface and internal amplitudes and experience more rapid azimuthal rotation as a function of distance from the jet surface, and thus have a much lesser effect on jet dynamics.

Dynamical behavior at early times in these equilibrium jet simulations is not likely to be indicative of the dynamics of astrophysical jets. This is because information about perturbations occurring at a jet's origin propagates outward along an astrophysical jet at speeds equal to or greater than the ram-pressure speed associated with the jet's leading edge. However, the final quasi-steady state achieved by the end of an equilibrium jet simulation, if parameters are appropriate to an astrophysical jet and the immediately surrounding external medium with which the jet interacts, should accurately represent the quasi-steady state achieved by an astrophysical jet far behind the jet front and any associated leading edge shock. If astrononically observed emission features correspond to the hotter compressive regions in the simulations, the present simulations have a number of astrophysical implications.

A robust conclusion that we can draw from the present two simulations is that FR II higher power radio sources and their accompanying jets must have significantly different parameters from those we have investigated here. It should be noted that our simulated jets disrupt on much shorter scale lengths than is the case in FR II radio sources. It seems more likely that our two present simulations share some of the aspects of the lowest power FR I type radio sources—for example, the jets in M84 (Bridle & Perley 1984; Laing & Bridle 1987), which show rapid broadening like the broadening seen in the Mach 5 jet simulation or the jet in M87 which is observed to dissipate rapidly after recollimating at knot. A. We have compared the observed broadening and slowdown of the jet in the Mach 5 simulation with the broadening and slowdown predicted to arise as a result of mass entrainment and turbulence as applied by Bicknell to FR I radio sources. In general, his models assume that the adiabatic effects of turbulence dominate the dissipative effects. Our present results indicate that significant spreading and slowdown of a light supersonic jet do not begin until the larger scale instabilities have grown to large amplitudes and presumably generated turbulence throughout much of the jet. Our present results also indicate that subsequent mass entrainment and jet broadening occur in the presence of transonic turbulence and weak shocks, and the observed broadening rate and jet slowdown are indicative of significant dissipation. At this point the implications for the FR I radio source models developed by Bicknell and for the deduced physical properties of jets in Bicknell et al. (1990) are unclear, but it is clear that the role of dissipative effects needs to be considered at least for light jet models with Mach numbers in excess of about 3.

Our present results also suggest that the presence of a driving frequency will couple helical and elliptical modes in such a way that one helical twist would correspond to one 360° rotation of the major axis of elliptical distortion. In general, this wavelength is significantly less than that associated with the fastest spatial growth of the elliptical mode. Thus, an elliptical twist not coupled to a helical twist may be indicative of random perturbations at the origin, and modes may grow independently at the fastest spatially growing wavelength. If the modes were to grow completely independently, the major axis of the fastest spatially growing elliptical distortion would rotate through 360° in a wavelength about 1.5 times longer than the fastest spatially growing helical twist. On an astrophysical jet, elliptical distortion will appear as a narrowing (brightening) and broadening (dimming) of emission due to line-of-sight effects through the emitting material, or as the twisting of an emission filament pair, since the simulations show that the ends of the major axis of elliptical distortion are marked by compressions. We note that the jet in M87 (Owen, Hardee, & Cornwell 1989) appears to go from broad (knot A) to narrow (between knots B and C) to broad (knot C). The observed morphology could be produced by an elliptical distortion that twists through 180° on a length scale comparable to that of the helical twist suggested by the sinusoidal oscillation of the jet in the plane of the sky between knots A and C. Thus, our present results would suggest that this jet is not subject to a dominant driving frequency at the origin. The tightly twisted filamentary structures such as those that appear on the M87 jet probably occur in a surface layer as suggested by the observations of Owen et al. (1989). We infer this from the simulations which show that the relatively tightly twisted surface features seen in velocity divergence images in the simulations appear to arise in a surface layer.

In order for jets to propagate to a large distance, the jets must overcome the problem posed by rapid filamentation, and the subsequent mass entrainment and shock heating which in the present simulations have led to jet slowdown. The fact that the higher Mach number simulation appears to spread faster than the lower Mach number simulation indicates that just raising the Mach number alone is not a complete solution. Some advantage will be gained by jet expansion in response to a declining atmospheric pressure, as was the case in two-dimensional simulations, but once the largest scale instabilities have reached large amplitude, tight collimation is not expected if large amounts of external material are entrained. In radio sources the creation of a large radio lobe requires a high-power jet much less dense than the undisturbed medium (Norman et al. 1984), and the high-power jet is then denser than the lobe or cocoon through which it flows. Thus, in high-power radio sources the jet would entrain considerably less material than in the present simulations. Presumably this will allow the jet to propagate much farther even after the development of large-scale instabilities. This implies that high-power jets protect

themselves through the creation of a lobe or cocoon of lower density than the jet, and this factor along with possibly higher Mach number and jet expansion in response to external pressure gradients probably allows them to propagate to the large observed distances. This contrasts with the low-power jets such as those in the FR I type radio sources which often do not appear to have formed extensive lobes or cocoons and may interact with a medium immediately external to the jet of comparable or greater density, such as we have investigated in the present simulations.

Although our present simulations do not compare quantitatively with FR II type radio jets, they do reproduce at least qualitatively some features seen on these jets. For example, the jet in Cygnus A (Dreher, Carilli, & Perley 1987) shows evidence for helical twisting. The jet also shows evidence for elliptical distortion that in emission appears to bifurcate the jet into a twisted filament pair. The filaments appears to twist through 180° on a length scale comparable to that of the helical twist suggested by the sinusoidal oscillation of the jet in the plane of the sky. Unlike the jets in the present simulations, the jet in Cygnus A does not disrupt as a result of the apparent bifurcation, and a relatively large-amplitude inferred helical twist is present. A second example of a feature observed in an FR II jet that may be similar to a feature in the simulations is the observation of side-to-side oscillation of emission contours within the jet in NGC 6251 (Perley, Bridle, & Willis 1984), where the whole jet apparent oscillation wavelength is $\sim 17.5R$ and the oscillation wavelength of interior emission contours is $\sim 5R$ (Hardee & Norman 1989). The present simulations suggest that the first helical body mode will twist the inner jet with a helical wavelength of one-quarter to one-fifth that of the fastest spatially growing whole jet helical twist. While our velocity divergence images do not reveal a strong compressive feature associated with the first helical body mode, it may be that such a feature is masked in our images by strong surface compressions. Certainly the sideways motion of the inner portion of the jet at nearly the jet sound speed observed in the simulations must be induced by relatively strong helically twisted high- and low-pressure regions inside the jet, and thus some oscillation of emission contours might be expected.

A difficulty in comparisons among theory, simulation, and observed jets is due in part to an uncertain relation between dynamical variables and observed emission features, e.g., an observationally defined jet radius and a dynamical jet radius. Note that the jet radius provides the fundamental length scale. A second difficulty occurs because structure may be induced by random perturbations or some driving frequency at the jet origin, e.g., a helical twist may arise from precession or orbital motion associated with the central power source or as the result of random perturbations. At least if opposed jets are present in an astrophysical system, this issue may be resolved by comparing the opposed jets. S-type large-scale structure about the central engine would indicate the presence of a precessional motion, and C-type structure would indicate the presence of an orbital motion of the central engine. The absence of S- or C-type structure in opposed jets would indicate random perturbations. If structures arise as the result of random perturbations at the jet origin and many frequencies are equally excited, then the observed wavelengths can behave differently from that associated with a dominant driving frequency. For example, along an expanding jet, spatial growth of helical twisting continues provided that $\omega < 1.5\omega^*$. Now $\omega^* \approx 1.3\ (a_x/R)$ provided that $M_{x,j} \gg 1$, and any frequency $\omega < 1.5\omega^* \sim 2(a_x/R)$, where (a_x/R) is the local value along the jet, can grow spatially (Hardee et al. 1994). At any location along the expanding jet the maximum spatial growth approximately corresponds to the local resonant frequency ω^* and to the associated wavelength λ^* as locally higher frequencies and shorter wavelengths grow more slowly or are no longer growing. The transverse displacement associated with wavelength λ^* can be $\approx R$, at which point transverse motions are on the order of the jet sound speed. The observed helical wavelength should then increase at least as fast as R because $\lambda^* \approx 6M_jR/(M_j + M_x)$. This is not the case for fixed driving frequency associated with precession or orbital motion, where the wavelength may actually decrease relative to the instantaneous jet radius. In this case the transverse displacement can grow nonballistically along the jet as long as $\lambda(\omega) > \lambda(1.5\omega^*)$, where once again $\omega < 1.5\omega^* \sim 2(a_x/R)$ and (a_x/R) is the local value along the jet. The transverse displacement can grow nonballistically up to a maximum on the order of $(\lambda/\lambda^*)R$, at which point transverse motions are on the order of the jet sound speed.

It is the observation of features on astrophysical jets such as helical twisting, elliptical distortion, dual filamentation, and helically twisted surface filaments that has provided the motivation for studying the dynamical stability properties of jet flow. The analytical theory has predicted that such structures should be an expected feature of jet flow and provides an estimate of the density and Mach number dependence of the expected dynamical features. While the linear theory provides clues as to the expected dominant dynamical features, the linear theory does not reveal how such features are modified as amplitudes grow large. However, the numerical simulations provide a test of the theoretically predicted features and provide the nonlinear modifications to such features. Ultimately, numerical simulation combined with aspects of the theory verified by the simulations can be used to model observed features on astrophysical jets and to extract fundamental parameters.

5. SUMMARY

In this paper we have compared two three-dimensional equilibrium jet simulations with each other and with predictions made by stability theory. The most important results are summarized below.

1. The simulations show that fluid displacements associated with helical, elliptical, and triangular surface modes play the dominant role in jet dynamics, in agreement with the theoretical prediction of lower amplitudes for higher order surface modes.
2. The simulations show that helical and elliptical surface modes triggered by a driving frequency are nonlinearly coupled.
3. Fluid displacements associated with body modes are theoretically predicted to decrease in amplitude and rotate rapidly in azimuth relative to the surface displacement as the jet axis is approached. Associated density and pressure maxima twist helically around the jet axis. Only the helical body modes produce nonzero displacement along the jet axis. Higher order body modes are predicted to be of lower amplitude.
4. The simulations show that the first helical body mode significantly twists an inner part of the jet at the predicted

maximally growing wavelength, and is not coupled to the driven helical surface mode.

5. Helical surface and first body modes and the elliptical surface mode observed in the simulations appear to be converged at the present grid resolution.

6. Significant mass entrainment begins only as the jet bifurcates or trifurcates as the result of nonlinear development of elliptical or triangular surface modes.

7. Shock heating accompanying mass entrainment is a significant factor in dissipation of directed jet energy at internal Mach numbers greater than about 3.

P. E. H. acknowledges support from the National Science Foundation through grant AST-8919180 and EPSCoR grant OSR-9108761 to the University of Alabama. D. A. H. was supported in the summer of 1993 by the National Science Foundation through REU grant AST-9300413 to the University of Alabama. D. A. C. acknowledges support from the Natural Sciences and Engineering Research Council of Canada (NSERC). The numerical work utilized the Cray 2 system at the National Center for Supercomputing Applications at the University of Illinois at Urbana-Champaign.

REFERENCES

Balsara, D. S., & Norman, M. L. 1992, ApJ, 393, 631
Bicknell, G. V. 1984, ApJ, 286, 68
———. 1986a, ApJ, 300, 591
———. 1986b, ApJ, 305, 109
Bicknell, G. V., de Ruiter, H. R., Fanti, R., Morganti, R., & Parma, P. 1990, ApJ, 354, 98
Birkinshaw, M. 1991, in Beams and Jets in Astrophysics, ed. P. A. Hughes (Cambridge: Cambridge Univ. Press), 278
Bridle, A. H., & Perley, R. A. 1984, ARA&A, 22, 319
Clarke, D. A. 1993, in Jets in Extragalactic Radio Sources, ed. H.-J. Röser & K. Meisenheimer (Berlin: Springer), 243
Clarke, D. A., Norman, M. L., & Burns, J. O. 1989, ApJ, 342, 700
Cox, C. I., Gull, S. F., & Scheuer, P. A. G. 1991, MNRAS, 252, 558
Dreher, J. W., Carilli, C. L., & Perley, R. H. 1987, ApJ, 316, 611
Hardee, P. E. 1983, ApJ, 269, 94
———. 1987, ApJ, 313, 607
Hardee, P. E. & Clarke, D. A. 1992, ApJ, 400, L9
Hardee, P. E., Cooper, M. A., & Clarke, D. A. 1994, ApJ, 424, 126
Hardee, P. E., Cooper, M. A., Norman, M. L., & Stone, J. M. 1992a, ApJ, 399, 478
Hardee, P. E., & Norman, M. L. 1988, ApJ, 334, 70
———. 1989, ApJ, 342, 680
Hardee, P. E. 1990, ApJ, 365, 194
Hardee, P. E., Norman, M. L., Koupelis, T., & Clarke, D. A. 1991, ApJ, 373, 8
Hardee, P. E., White, R. E., III, Norman, M. L., Cooper, M. A., & Clarke, D. A. 1992b, ApJ, 387, 460
Laing, R. A., & Bridle, A. H. 1987, MNRAS, 228, 557
Norman, M. L. 1993, in Astrophysical Jets, ed. D. Burgarella, M. Livio, & C. P. O'Dea (Cambridge: Cambridge Univ. Press), 211
Norman, M. L., & Hardee, P. E. 1988, ApJ, 334, 80
Norman, M. L., & Winkler, K.-H. A. 1986, in Astrophysical Radiation Hydrodynamics, ed. K.-H. A. Winkler & M. L. Norman (Dordrecht: Kluwer), 187
Norman, M. L., Winkler, K.-H. A., & Smarr, L. L. 1984, in Physics of Energy Transport in Extragalactic Radio Sources, ed. A. H. Bridle & J. A. Eilek (Green Bank: NRAO), 150
Owen, F. N., Hardee, P. E., & Cornwell, T. J. 1989, ApJ, 340, 698
Payne, D. G., & Cohn, H. 1985, ApJ, 291, 655
Perley, R. A., Bridle, A. H., & Willis, A. G. 1984, ApJS, 54, 291
Stone, J. M., & Norman, M. L. 1992a, ApJS, 80, 753
———. 1992b, ApJS, 80, 791
van Leer, B. 1977, J. Comput. Phys., 23, 276
Zhao, J-H., Burns, J. O., Hardee, P. E., & Norman, M. L. 1992a, ApJ, 387, 69
Zhao, J-H., Burns, J. O., Norman, M. L., & Sulkanen, M. E. 1992b, ApJ, 387, 83